ELSEVIER

Contents lists available at ScienceDirect

International Journal of Plasticity

journal homepage: www.elsevier.com/locate/ijplas





A dislocation theory-based model for brittle-to-ductile transition in multi-principal element alloys

Zebin Han^a, Bin Liu^b, Qihong Fang^{a,*}, Peter K Liaw^c, Jia Li^{a,*}

- a State Key Laboratory of Advanced Design and Manufacturing Technology for Vehicle, Hunan University, Changsha 410082, PR China
- ^b State Key Laboratory of Powder Metallurgy, Central South University, Changsha 410083, PR China
- ^c Department of Materials Science and Engineering, The University of Tennessee, Knoxville, TN 37996, USA

ARTICLE INFO

Keywords: Multi-principal element alloys Brittle-to-ductile transition Yield strength Brittle-to-ductile transition temperature

ABSTRACT

Multi-principal element alloys (MPEAs) have drawn great interest due to their superior mechanical properties compared to the conventional alloys. However, it is unclear in these two aspects: i) how to predict the brittle-to-ductile transition temperature (BDTT) and fracture toughness of MPEAs using theory and model; ii) how to quantify the influences of the complicated alloy composition variation and microstructural parameter on the BDTT and fracture toughness of MPEAs. These issues are critical to both the underlying mechanisms and practical engineering applications. Here, we develop a dislocation theory-based model accounting for the modified lattice friction stress model, the composition-dependent strength model, and the critical energy model to determine the BDTT and corresponding fracture toughness in body-centered cubic MPEAs. The calculated yield stress and BDTT of the as-cast MPEA agree well with the experiments. Subsequently, the BDTT and fracture toughness of TiVNbTa-based MPEAs are obtained as a function of the element concentration fluctuation. The effects of microstructure parameters, such as component randomness and short-range ordering described by the standard deviation of the interplaner potential perturbation and short-range correlation length, on the BDTT and fracture toughness are further elucidated. Importantly, a microstructure-based BDT criterion is proposed to evaluate whether MPEA is ductile or brittle at a given temperature. These results are conducive to the development and application of MPEAs in extreme environments.

1. Introduction

Multi-principal element alloys (MPEAs) have excellent mechanical properties, such as high strength, good ductility, structural stability, and wear resistance (George et al., 2019; Li et al., 2022a; Miracle and Senkov, 2017; Rao et al., 2022; Senkov et al., 2018; Ye et al., 2016; Zhang et al., 2024, 2015). They are composed of multiple elements in equimolar or approximately equimolar proportions (Cantor et al., 2004; Mak et al., 2021; Santodonato et al., 2015; Yeh et al., 2004). The high mixing entropy of MPEAs reduces the Gibbs free energy, and hinders the formation of intermetallic phases (Li et al., 2020; Senkov et al., 2015, 2014; Soler et al., 2018). Thus, MPEAs tend to show single-phase solid solutions, including face-centered cubic (FCC) and body-centered cubic (BCC) structures. A major class of MPEAs is the Cr-Mo-Nb-Ta-V-W-Hf-Ti-Zr family of BCC alloys, which have high yield strength and high temperature strength retention (Senkov et al., 2014).

E-mail addresses: fangqh1327@hnu.edu.cn (Q. Fang), lijia123@hnu.edu.cn (J. Li).

https://doi.org/10.1016/j.ijplas.2024.104059

Received 4 March 2024; Received in revised form 29 June 2024;

Available online 14 July 2024

0749-6419/© 2024 Elsevier Ltd. All rights are reserved, including those for text and data mining, AI training, and similar technologies.

^{*} Corresponding authors.

In recent years, the mechanical properties of MPEAs have been extensively studied by combining experiments, theoretical models, with computational simulations (Zhang et al., 2023a). For instance, based on the theoretical guidance and thermodynamic tools, an alloy design process is proposed to discover new single-phase BCC refractory MPEAs that satisfy specific mechanical properties (Rao et al., 2022). Based on the understanding of traditional refractory metals and alloys, the influence of the interstitial compositions on the mechanical properties of refractory complex concentrated alloys has been thoroughly investigated (Belcher et al., 2023). According to the classical Peierls-Nabarro (P-N) model, a stochastic P-N model has been proposed to explain the origin of high strength in MPEAs (Zhang et al., 2019a). The decomposition of the BCC structure into $\beta+\beta^*$ through the spinodal decomposition produces a modulation of the chemical composition, which achieves an excellent combination of strength 1.1 GPa and ductility 28 % in HfNbTiV MPEAs (An et al., 2021). Combining the first-principles calculations and a set of physical descriptors, the surrogate models are developed to find the candidate alloys that have the enhanced strength-ductility synergies (Hu et al., 2021). The addition of the W element increases the vield stress of TiZrHfNbTa MPEAs from 1064 MPa to 1726 MPa for TiZrHfNbTaW MPEAs (Huang et al., 2022). Based on the theoretical model, the effect of the severe lattice distortion on the mechanical properties reveals that the influence of the atomic-radius mismatch on the solid-solution strengthening is the primary factor to govern the yield stress in the BCC AlxHfNbTaTiZr MPEA, surpassing the impact of the shear-modulus mismatch (Li et al., 2020). The orientation-dependent tensile behavior of HfNbTaTiZr MPEAs, the characteristics of deformation twinning, and phase transformations have been investigated at the nanoscale using molecular dynamics (MD) simulations (Jian and Ren, 2024). The above work has made crucial progress in elucidating the close connection between the components, microstructures, and mechanical properties in MPEAs.

There are new theoretical advances to study the fracture behaviors and failure mechanisms (Guo et al., 2024; Li et al., 2022b; Shen et al., 2024; You et al., 2021; Zhao et al., 2023). In terms of the theory of the brittle-ductile transition (BDT) of metals and alloys, the effect of the crack extension on the BDT behavior is emphasized in the previous work (Heslop and Petch, 1956, 1958). It is considered that the BDTT is decided by the P-N stress associated with a free dislocation. The BDT behavior of metals is studied by the mechanism of dislocation source nucleation, which is controlled by dislocation mobility at a constant loading rate (Hirsch and Roberts, 1996; Hirsch et al., 1989). The fracture toughness and the BDTT in the as-cast TiVNbTa MPEA are measured by conducting four-point bending tests at temperatures ranging from - 139 °C to 20 °C and a strain rate of 1×10^{-3} s⁻¹ (Scales et al., 2020). Based on the competition between dislocation source operation and crack extension, an analytical method to calculate the BDTT is proposed in the pure metals (Zhang et al., 2019b). The ratio of the screw dislocation velocity to edge dislocation velocity is regarded as a controlling factor to the BDT (Lu et al., 2021). A probabilistic model that incorporates temperature-dependent constitutive relationships has been developed to accurately describe the competition between cleavage and ductile void failure. This model successfully predicts the temperature-dependent fracture toughness and the BDTT in ferritic steels with irradiation effects (Chen et al., 2020). A quantum-mechanical dimensionless metric is proposed to accurately predict the ductility of various MPEAs. This metric aligns well with results from existing tensile experiments (Singh et al., 2023). A room temperature ductility criterion, namely, the ratio of the stress intensity factor for dislocation emission to the stress intensity factor for cleavage, is proposed to analyze the ductility of the existing MPEAs (Mak et al., 2021). Based on a unified thermodynamic framework, a coupled crystal plasticity and phase field model is proposed to study the BDT process and predict the experimental results well in the pure W (Li et al., 2022b). The crystal plasticity models have been used to reveal the temperature dependence of deformation localization in the irradiated W (Li et al., 2021b). A discrete-continuum model, combining 3D discrete dislocation dynamics with the finite element method, provides an effective way to understand the behavior of high-speed dislocations under the complex shock loading conditions (Cui et al., 2022). In addition, the role of slow screw dislocations on the fast strain burst events in submicron W is studied using the discrete dislocation dynamics simulations, and the results show the external load mode control can transform the complex collective dynamics of dislocations (Cui et al., 2016, 2020). Through different methods, the previous studies have made significant progress in understanding the deformation behavior and BDT of the alloys.

While there have been recent significant theoretical advancements that explain the relationship between yield stress and composition in BCC MPEAs, there is a significant lack of research on ductility properties, such as BDTT and fracture toughness (Mak et al., 2021). The alloying elements and interstitial impurities have a significant effect on the BDTT (Scales et al., 2020; Zhang et al., 2020). The chemical short-range ordering (SRO) has been observed in the atomic simulations and experimental studies (Chen et al., 2021a, 2021b; Körmann et al., 2017; Li et al., 2019; Singh et al., 2015; Tamm et al., 2015). The previous research has demonstrated that SRO has the potential to enhance the strength of the alloy (Jouiad et al., 1999; Li et al., 2023b; Pettinari-Sturmel et al., 2002). The SRO plays an impact on the dislocation friction stress based on the classic P-N model. The potential strengthening mechanism involves increasing the volume of mismatch, facilitating dislocation cross-slip and multiplication, and phase transformation (Wu et al., 2021). In addition, the interaction between dislocation and SRO has a significant impact on the thermal activation process of dislocation slip (Tanaka et al., 2012). With an increase in the Cu content, the low SRO degree decreases the activation energy required for dislocation slip, ultimately lowering the BDTT in the FeCrNCu MPEA (Tanaka et al., 2014). However, there is a lack on the quantitative impact of SRO on the BDTT and fracture toughness in the MPEA.

In the present work, a dislocation theory-based model is developed to quantify the influence of the alloying element and SRO on the dislocation motion, BDTT, and fracture toughness in MPEAs. The developed model gives a quantitative prediction for the compositional contribution to the BDTT and fracture toughness. In addition, the microstructure-based brittle-ductile transition criteria is proposed.

2. Modeling and theory

The distinction between ductile and brittle fracture in crystalline metals is primarily determined by whether or not yielding occurs. In essence, the brittle fracture typically occurs prior to yielding, whereas ductile fracture occurs after the metal has yielded. In the case

of polycrystalline materials, stress concentrations caused by clusters of dislocation pile-ups can trigger dislocation sources in neighboring grains and facilitate crack propagation. If the crack propagation is the primary initiation process, fracture occurs before yielding, resulting in a brittle fracture. On the other hand, if the dislocation source is initiated first, fracture occurs after yielding, leading to a ductile fracture. The dislocation mechanism theory is widely adopted to investigate the BDT behavior (Bonnekoh et al., 2019; Heslop and Petch, 1956, 1958; Lu et al., 2021; Petch, 1958; Zhang et al., 2023b), which depends on grain size, lattice friction stress, yield strength, and applied stress. Hence, the models of dislocation friction stress and yield strength are determined in MPEAs due to their complex element composition and distribution. For example, from the previous experiments (Chen et al., 2024; Zhu et al., 2024), MPEAs have a random distribution or locally chemically ordered distribution of atom types at several nanometers, leading to atomic severe lattice distortion. However, the classic P-N model hardly predicts the dislocation friction stress due to the constantly changing lattice parameters at several nanometers. Thus, the theoretical framework is established in this work for BDT based on the dislocation mechanism-based critical energy model.

2.1. Dislocation mechanism-based critical energy model

Here, the BDT depends on the competition between crack propagation priority and crack tip dislocation source activation priority in MPEAs. The ductile fracture occurs when the dislocation source firstly operates, and the brittle fracture takes place when the crack begins to extend. Fig. 1 shows a reasonable model from the previous experiment for crack propagation and dislocation pile-up in the adjacent grains of CrMnFeCoNi MPEAs (Suzuki et al., 2020).

Hence, the effective potential barrier for the initiation of dislocation sources at the crack tip in the MPEA is

$$E = E_1 + E_3 - E_2 - E_4 \tag{1}$$

where E_1 is the energy for the dislocation line tension, E_2 is the consumed energy for the dislocation movement, E_3 is the energy of the

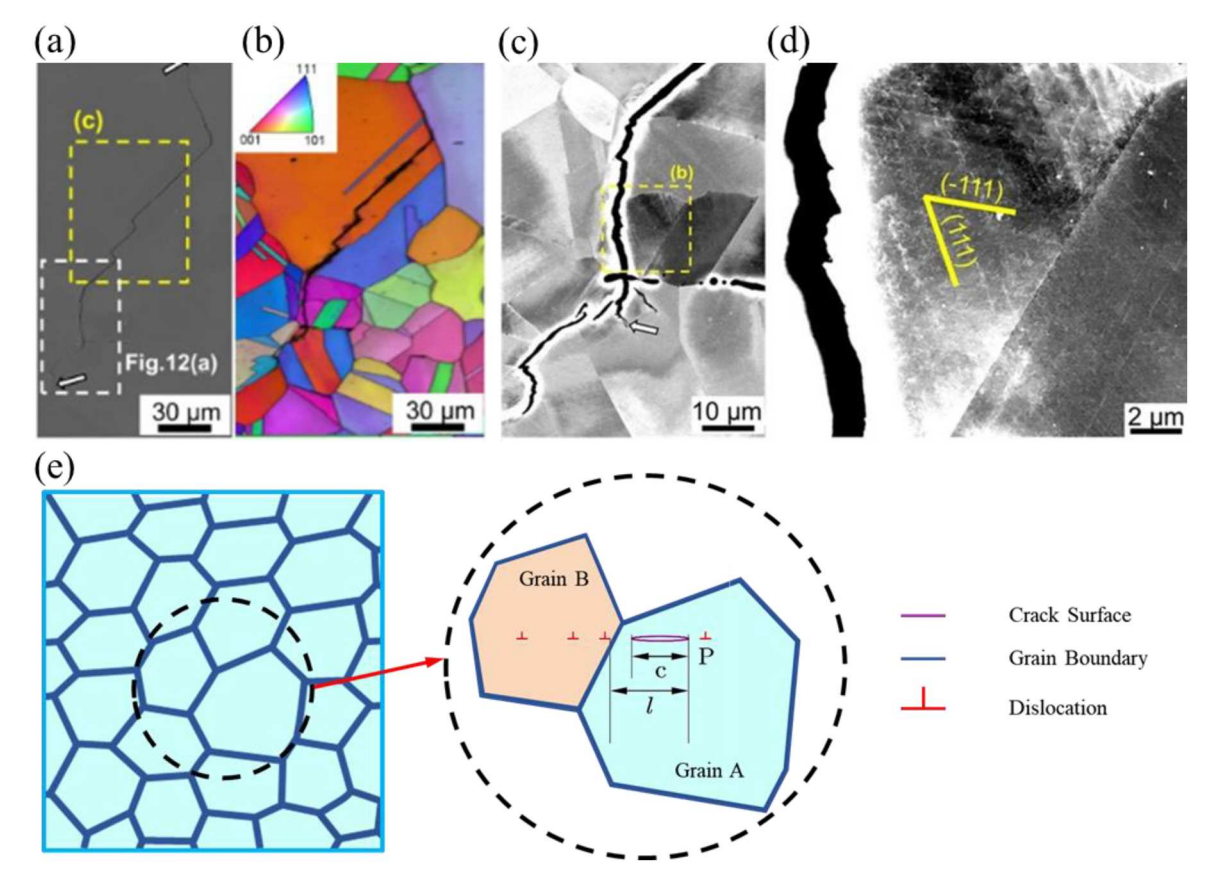


Fig. 1. (a) Overview around one of the subcracks near the main crack in the CrMnFeCoNi MPEA. (b) The corresponding Inverse Pole Figure map. (c) Magnified electron channeling contrast images of the crack initiation site. (d) Dislocation pile-up. (a-d) come from previous work (Suzuki et al., 2020). (e) The schematic diagram of two adjacent grains in MPEAs containing a crack. The length of the crack is *c*, the distance between the pile-up position and the crack tip is *l*, and the dislocation source exists at the point, P, in the front of the crack tip. Assuming that a large amount of slipping dislocations pile-up on the boundary between grains A and B.

crack propagation, and E_4 is the crack surface energy (Zhang et al., 2019b). When the thermal activation energy overcomes the maximum effective potential barrier, the BDT behavior occurs.

The energy for the dislocation line tension is

$$E_1 = F\theta b \tag{2}$$

where $F = \mu b^2 / 2$ is the line tension. μ is the shear modulus. θb is the elongation of the arc "CD". Here, the dislocation segment "CD" is expanded from the radius r_1 to radius r_2 , as shown in Fig. 2.

The consumed energy for the dislocation segment "CD" movement is expressed as

$$E_2 = \sigma b \Delta S$$
 (3)

$$\sigma = (\sigma_{\mathbf{v}} - \sigma_{\mathbf{f}})(d/l)^{\frac{1}{2}} \tag{4}$$

$$\Delta S = \frac{1}{2} \left(\pi r_2^2 \frac{\theta}{2\pi} - \pi r_1^2 \frac{\theta}{2\pi} \right) \approx \frac{\theta b r_2}{2} \tag{5}$$

where σ is the amplified stress of the pile-up group at the point of P, ΔS is the area of the pink area swept by the dislocation source. σ_{y} is the yield stress, which is given by Eq. (24). $\sigma_{f} = M(\sigma_{PN} + \tau_{1} + \tau_{2} + \tau_{3})$ is the stress acted on the dislocation motion, where σ_{PN} is determined by Eqs. (22, 23). τ_{1} is the stress of the elastic interaction with other dislocations, τ_{2} is the stress of the jogs formation, and τ_{3} denotes the stress of the elastic stress field of the dislocation. Here, $\tau_{i} = \alpha_{i}\mu b/x$, α_{i} is approximately between 0.2 and 0.3. The value of x is approximately 10^{-7} m. d is the average grain size. The radius r_{2} is expressed by $r_{2} = m/[2\sin(\theta/2)]$.

The elastic energy released by crack expansion for plane stress conditions is approximated as $U = \pi \sigma^2 cb^2/(2\mu)$ (Lawn, 1993). When the dislocation source opens first at point P, the unreleased elastic energy will become the energy barrier for the dislocation source to open. Thus, the energy of the crack propagation is

$$E_3 = \frac{\pi \sigma^2 c b^2}{2u} \tag{6}$$

The surface energy of the crack is

$$E_4 = 2b^2\gamma_{\rm c} \tag{7}$$

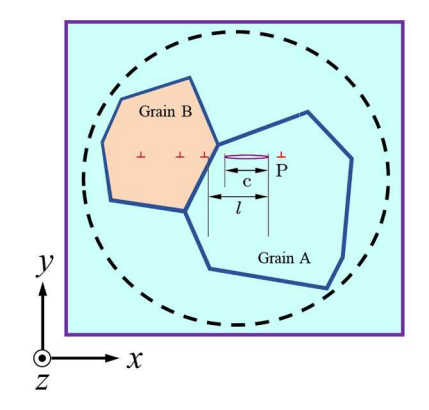
where $2b^2$ is the incremental crack surface area, and γ_s is the specific surface energy. Here, the crack extends from c to c+b. The relationship between strain rate and BDTT has been determined by (Tanaka et al., 2008)

$$\dot{\varepsilon} = A e^{-E_a/(kT_c)} \tag{8}$$

where $\dot{\varepsilon}$ is the strain rate, A is a pre-factor, E_a is the activation energy for the BDT behavior, k is the BDTT.

According to the thermal activation theory, the strain rate can be given by (Argon, 2007)

$$\dot{\varepsilon} = \rho b s v_d e^{-E_a/(kT_c)} \tag{9}$$



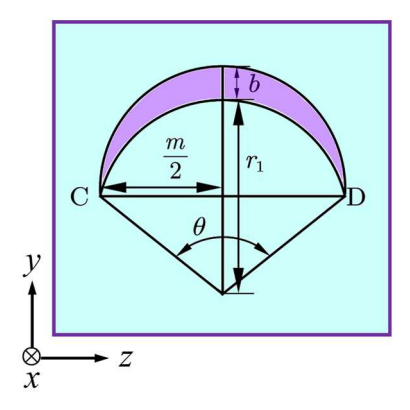


Fig. 2. The schematic diagram of the curved segment of dislocation at the point, P, in the front of the crack tip. The dislocation source is supposed to be a segment of dislocation with a Burgers vector, b, and length, m, where the ends are fixed at points C and D. The dislocation segment, denoted as "CD", bends under the applied stress, and the arc "CD" corresponds to a circular angle of θ ($0 < \theta \le \pi$); the radii before and after the moved distance b in the top of "CD" are r_1 , and r_2 , respectively. It is assumed that the center angle of the dislocation is the same before and after it moves a distance b, thus $r_2 = r_1 + b$.

where ρ is the mobile dislocation density, b is the Burgers vector, s is the dislocation moved distance, and v_d is the natural vibration frequency of the dislocation.

Thus, the BDTT is

$$T_c = \frac{E_{\text{max}}}{k[\ln(b^2 \rho v_d) - \ln(\dot{\varepsilon})]}$$
(10)

where $E_{\text{max}} = E_1 + E_3 - E_2 - E_4$ is the maximum energy change at $\theta = \pi$.

The fracture toughness of metallic materials varies with the temperature. When the temperature is below the BDTT, the fracture toughness decreases rapidly. In the temperature-transition region, the relationship between the fracture toughness and temperature is (Sailors and Corten, 1972)

$$K_{\rm IC} = k_1 \chi^{0.5} \tag{11}$$

$$\chi = \chi_0 / [1 + e^{-B(T - T_c)}] \tag{12}$$

where $K_{\rm IC}$ is the fracture toughness, the constant k_1 is 14.6, χ is the Charpy V-notch value, χ_0 and B are obtained from the experimental data, and T is the temperature.

2.2. Dislocation friction stress

The dislocation core plays an important role in the dislocation slip and dislocation interaction (Alkan et al., 2018; Fan et al., 2021; Krasnikov and Mayer, 2018; Li et al., 2021a; Yang et al., 2020). In the classical P-N model (Nabarro, 1947; Peierls, 1940), it integrates an atomic-level description of dislocation core and a long-range description of the dislocation strain field (Hirth et al., 1983). Fig. 3 shows a single edge dislocation in MPEAs, and this model considers the random atom occupancy and SRO (Zhang et al., 2019a).

The total energy, stress field, misfit energy, and generalized stacking-fault energy (GSFE) in a single edge dislocation are given by (Anderson et al., 2017)

$$E_{\text{total}} = \frac{1}{2} \int_{-\infty}^{+\infty} \sigma_{yx}(\mathbf{x}) \varphi(\mathbf{x}) d\mathbf{x} + E_{\text{misfit}}$$
(13)

$$\sigma_{yx}(x) = \frac{\mu}{2\pi(1-\nu)} \int_{-\infty}^{+\infty} \frac{\varphi'(x_1)}{x - x_1} dx_1$$
 (14)

$$E_{\text{misfit}} = \int_{-\infty}^{+\infty} \gamma[\varphi(x)] dx \tag{15}$$

$$\gamma(\varphi) = \frac{\mu b^2}{4\pi^2 a} \left(1 - \cos \frac{2\pi \varphi}{b} \right) \tag{16}$$

where $\sigma_{yx}(x)$ is the shear stress on the slip surface, ν is the Poisson ratio, and $\gamma(\varphi)$ is the periodic interplanar potential. Assuming that the dislocation line in a grain of MPEAs is along the z-axis and the Burgers vector is along the x-axis, and the slip plane is the x-z plane. Two continuous and linear elastic half spaces (y>0) and y<0 are separated by the slip plane. The disregistry function in the x direction along the slip plane is expressed by a function, $\varphi(x)$; $\varphi(x\to -\infty)=0$ and $\varphi(x\to +\infty)=b$. The distribution of the disregistry is $\varphi(x)=\varphi'(x)$. α is the spacing of the atomic plane perpendicular to the glide plane.

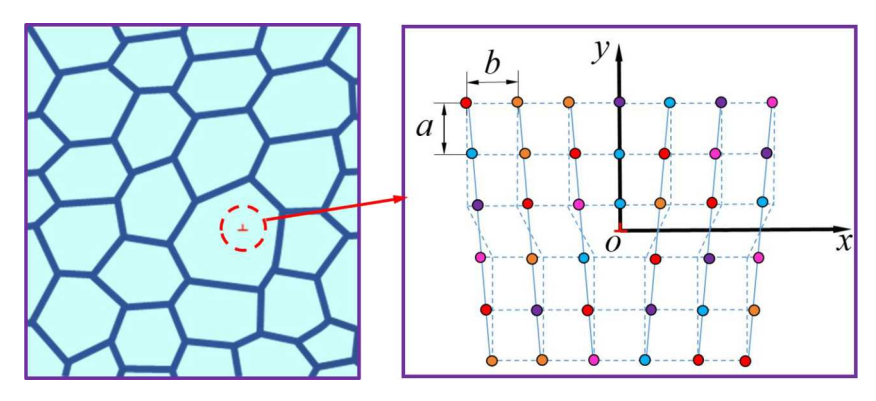


Fig. 3. The schematic diagram of an edge dislocation in a grain of MPEAs formed by the simple cubic crystals. Although MPEAs have severe lattice distortion, we plot it as a simple cubic lattice for simplicity.

The equilibrium dislocation disregistry function and core width are derived by $\delta E_{\text{total}}/\delta[\varphi(x)]=0$. The disregistry function and Peierls stress are expressed as follows

$$\varphi(x) = \frac{b}{\pi} \arctan \frac{x}{w_0} + \frac{b}{2} \tag{17}$$

$$\sigma_p^0 = \mu \exp\left(-\frac{2\pi w_0}{h}\right) \tag{18}$$

where $w_0 = a/[2(1-\nu)]$ is the dislocation core width.

In MPEAs, the random lattice occupancy varies from the site to site, and thus the misfit energy related to the GSFE is different from that of traditional alloys. To understand the effect of the random site occupancy and SRO on the intrinsic strength, a random variable, $\overline{\omega}(x)$, with the short-range spatial correlation is introduced. Thus, the misfit energy is expressed as

$$E_{\text{misfit}} = \int_{-\infty}^{+\infty} \overline{\omega}(x) \gamma(\varphi(x)) dx \tag{19}$$

The random variable is described by a normal distribution, and its probability density function is

$$P_{\overline{w}}(u) = \frac{1}{\overline{\Delta}\sqrt{2\pi}} \exp\left(-\frac{(u-1)^2}{2\overline{\Lambda}^2}\right) \tag{20}$$

where $\overline{\Delta}$ is the standard deviation, and it is written as

$$\overline{\Delta} = \frac{2w_0}{\pi} \sqrt{\frac{2}{\lambda}} \Delta \sqrt{\int_{-\infty}^{+\infty} \left[\int_{s}^{+\infty} \exp\left(-\frac{x-s}{\lambda}\right) \frac{x^2}{\left(x^2 + w_0^2\right)^2} dx \right]^2 ds}$$
 (21)

Here, the standard deviation explicitly depends on the short-range spatial correlation λ and standard deviation Δ (Zhang et al., 2019a). The reasons for choosing a normal distribution are explained in Appendix A.

The dislocation friction stress and its probability distribution in the MPEA are expressed as

$$\sigma_{PN} = \sigma_{v}^{0} e^{\beta^{-1} \left(1 - \overline{\omega}^{-1}\right)} \tag{22}$$

$$P_{\bar{\sigma}_{c}}(u) = P_{\bar{\omega}}(1/(1-\beta\log u))(\beta/u)(1-\beta\log u)^{-2}$$
(23)

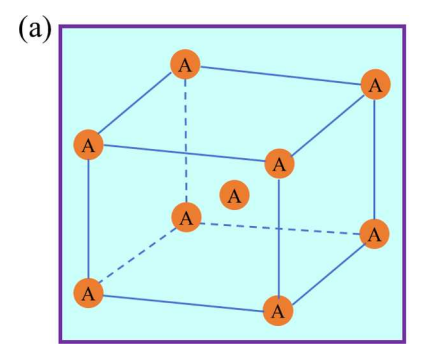
where $\beta = b/(2\pi w_0)$. Here, $\tilde{\sigma}_p$ is defined as the normalized dislocation friction stress, σ_{PN}/σ_p^0 . Therefore, the dislocation friction stress of a single edge dislocation is a function of the standard deviation of the GSFE perturbation and the correlation length of the spatial component distribution. Hence, the existence of SRO significantly influences the standard deviation of the GSFE perturbation and the correlation length of the spatial component distribution, thus ultimately impacting the dislocation friction stress.

2.3. Composition-dependent strength model

For a single-phase BCC MPEA, there are three strengthening mechanisms that contribute to the yield strength, including the solid-solution strengthening, σ_{ss} , dislocation strengthening, σ_{dis} , and grain-boundary strengthening, σ_{gb} . Hence, the yield stress in Eq. (4) for the MPEA is expressed as

$$\sigma_{y} = \sigma_{ss} + \sigma_{dis} + \sigma_{gb} \tag{24}$$

Solid-solution strengthening originates from various interactions between dislocations and solute atoms (Li et al., 2023c), including



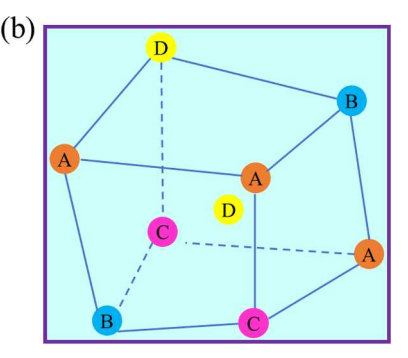


Fig. 4. (a) The schematic depiction of the pure BCC crystal structure. (b) The severely distorted crystal for four-principal-element BCC MPEAs.

elastic interaction, modulus interaction, electrical interaction, chemical interaction, and localized ordering interaction. Among these, the elastic interaction and modulus interaction dominate solid-solution strengthening (Courtney, 2005). Here, the contribution of SRO to the yield strength of MPEAs is very limited (Zhang et al., 2020). Previous work has suggested that the contribution of SRO only accounts for about 4 % of the yield strength of BCC MoNbTaW MPEA (Li et al., 2023a), and even SRO results in a decrease in the yield strength of solid solution alloys (Abu-Odeh and Asta, 2022). Moreover, the SRO causes the limited antiphase boundary strengthening (Schön, 2021), while it leads to a decrease in solute concentration which greatly reduces solid solution strengthening (Fang et al., 2022). On other hand, the antiphase boundary energy is very difficult to measure and calculate due to the formation of the complex SRO and the obvious changeable solute composition around the SRO structure, thus hardly evaluating the SRO contribution to the yield strength in MPEAs. As a result, this work primarily investigates the dominant solid-solution strengthening mechanism, while disregarding the weaker SRO strengthening effect.

Here, the solute atom in the BCC matrix induces the lattice distortion to impede dislocation motion (Fig. 4). Based on Vegard's law (Li et al., 2020; Toda-Caraballo and Rivera-Díaz-del-Castillo, 2015; Vegard, 1916), for MPEA composed with n elements, the contribution of solid solution strengthening to the yield stress is summarized as:

$$\sigma_{ss} = \sum_{i=1}^{n} c_i \sigma_{ss}^i \tag{25}$$

where c_i is the atomic percentage of the element, i. The strength contribution, σ_{ss}^i , of the element, i, is expressed as

$$\sigma_{ss}^{i} = A\mu c_{i}^{2/3} \delta_{i}^{4/3} \tag{26}$$

where A = 0.04 is the material constant, and $\mu = \sum_{i=1}^{n} c_i \mu_i$ is the shear modulus following the average rule (Senkov et al., 2010). The mismatch parameter, δ_i , is given by (Toda-Caraballo and Rivera-Díaz-del-Castillo, 2015)

$$\delta_i = \xi \left(\delta u_i^2 + \beta^2 \delta r_i^2\right)^{1/2} \tag{27}$$

where $\xi=2.5$ in BCC metals (Li et al., 2020), $\delta\mu_i$ is the shear modulus mismatch, and δr_i is the atomic-size mismatch. The coefficient β is dependent on the kind of dislocations (Labusch, 1970). For screw dislocations, $3<\beta<16$ is used, while for edge dislocations, $\beta>16$ is employed. MPEA, ijkl, is assumed to be composed of a multi-principal matrix, jkl, and an additional element, i. The expressions of the atomic-size mismatch, δr_i , as well as the modulus mismatch, $\delta \mu_i$, are given: $\delta r_i = \frac{\delta r_{ijkl}^{ane} - \delta r_{jkl}^{ane}}{c_i}$ and $\delta \mu_i = \frac{\delta \mu_{ijkl}^{ane} - \delta r_{ijkl}^{ane}}{c_i}$, δr_{ijkl}^{ane} are the average atomic size mismatch and average modulus mismatch of the ijkl MPEA, respectively. The expressions δr^{ave} and $\delta \mu^{ave}$ are calculated by

$$\delta r^{ave} = \sum_{i}^{n} \sum_{j}^{n} c_{i} c_{j} \delta r_{ij} = (c_{1}, c_{2}, \dots, c_{n}) \begin{pmatrix} \delta r_{11} & \delta r_{12} & \dots & \delta r_{1n} \\ \delta r_{21} & \delta r_{22} & \dots & \delta r_{2n} \\ \vdots & \dots & \ddots & \vdots \\ \delta r_{n1} & \delta r_{n2} & \dots & \delta r_{nn} \end{pmatrix} \begin{pmatrix} c_{1} \\ c_{2} \\ \vdots \\ c_{n} \end{pmatrix}$$

$$(28)$$

$$\delta\mu^{ave} = \sum_{i}^{n} \sum_{j}^{n} c_{i} c_{j} \delta\mu_{ij} = (c_{1}, c_{2}, \cdots, c_{n}) \begin{pmatrix} \delta\mu_{11} & \delta\mu_{12} & \cdots & \delta\mu_{1n} \\ \delta\mu_{21} & \delta\mu_{22} & \cdots & \delta\mu_{2n} \\ \vdots & \cdots & \ddots & \vdots \\ \delta\mu_{-1} & \delta\mu_{-2} & \cdots & \delta\mu_{-n} \end{pmatrix} \begin{pmatrix} c_{1} \\ c_{2} \\ \vdots \\ c_{n} \end{pmatrix}$$

$$(29)$$

where $\delta\mu_{ij}=2\left(\mu_i-\mu_j\right)/\left(\mu_i+\mu_j\right)$ and $\delta r_{ij}=2\left(r_i-r_j\right)/\left(r_i+r_j\right)$ are the shear-modulus mismatch and the atomic-size mismatch between two elements, i and j, respectively. μ_i and r_i are the shear moduli and atomic radii of the element, i. There are no atomic-size mismatch and shear-modulus mismatch between atoms i. Therefore, δr_{ii} and $\delta\mu_{ii}$ are zero. The probability of mismatch between atom i and atom j is c_ic_j .

According to the Taylor relationship (Kim et al., 2019), the dislocation strengthening is written as

$$\sigma_{
m dis} = M \varepsilon \mu b \sqrt{
ho}$$
 (30)

where M=3.06 is the Taylor constant, and $\varsigma=0.33$ is an empirical constant.

The grain boundary strengthening is written as (Liu et al., 2013)

$$\sigma_{\rm gb} = k_{\rm y} d^{-1/2} \tag{31}$$

where k_y is the Hall-Petch constant.

2.4. Microstructure-based brittle-to-ductile transition criterion

Based on Eqs. (2-7), the relationship between the effective potential barrier and microstructure is obtained as

$$E_{\text{max}} = \mu b^3 \pi / 2 + \pi c b^2 \sigma^2 / (2\mu) - \sigma m b^2 \pi / 4 - 2b^2 \gamma_s$$
 (32)

Hence, from Eqs. (10, 32), the microstructure-based BDT criteria can be expressed by

$$\frac{\pi c db^2}{2\mu l} f(d,\lambda,\Delta)^2 - mb^2 \pi \left(\frac{l}{d}\right)^{1/2} f(d,\lambda,\Delta) \left/ 4 + \frac{\mu b^3 \pi}{2} - 2\gamma_s b^2 - kT \left[\ln \left(b^2 \rho \nu_d \right) - \ln(\dot{\varepsilon}) \right] \le 0 \right. \tag{33}$$

where $f(d, \lambda, \Delta) = \sigma_y - \sigma_f$ is defined as the microstructure parameters. The microstructural parameters are influenced by various factors, including the average grain size, the standard deviation of the interplaner potential perturbation, and the short-range correlation length. In addition, Eq. (33) is simplified as

$$f(d,\lambda,\Delta) - \left(\frac{l}{d}\right)^{1/2} \frac{m\mu}{4c} \left[1 + \sqrt{1 + \left[kT \left[\ln\left(b^2 \rho \nu_d\right) - \ln(\dot{\varepsilon}) \right] + 2\gamma_s b^2 - \frac{\mu b^3 \pi}{2} \right] \frac{32c}{\pi \mu b^2 m^2}} \right] \le 0$$
 (34)

Here, for a given temperature T, when Eq. (34) is satisfied, the material is ductile; otherwise, the material is brittle.

Therefore, the BDT behavior is predicted in MPEAs based on the above developed physical model. Considering the critical energy model, the modified lattice friction stress model, and the composition-dependent yield strength model, Fig. 5 shows the flowchart of the calculation process for the dislocation theory-based model. It is important to note that the critical energy model based on dislocation theory is not dependent on the materials used. The modified lattice friction stress model takes into account the component randomness and SRO of MPEAs. Additionally, the composition-dependent strength model considers the effects of composition, lattice distortion, and component concentration in MPEAs. Therefore, the developed physical model provides accurate and reasonable predictions for the BDT behavior. The specific calculation details are described as follows: i) To begin with, we would provide definitions for the following parameters: atomic radii, shear modulus, atomic fractions, dislocation density, Hall-Petch constant, and grain size, as outlined in Eqs. (24-31). Subsequently, we will make predictions regarding the yield strength, taking into account solid-solution strengthening stress, grain-boundary strengthening stress, and dislocation strengthening stress. ii) Secondly, determine the dislocation friction stress using Eqs. (18-23). The average dislocation friction stress is determined by the phenomenological parameters Δ and λ . iii) Finally, predict the BDTT of MPEA of MPEA using Eqs. (1-10). As the composition of MPEA varies, the yield strength, shear modulus, and dislocation friction stress also vary, leading to changes in the effective potential barrier and ultimately influencing the BDTT.

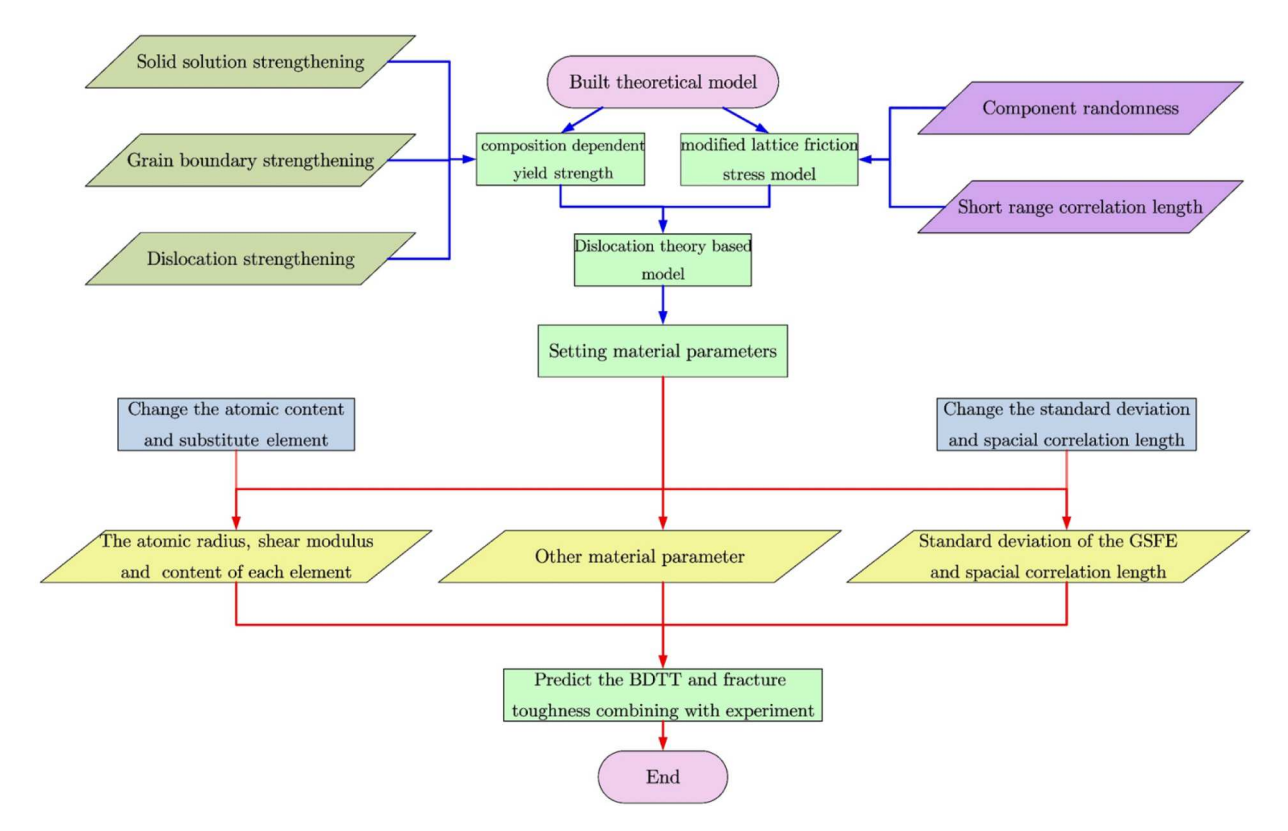


Fig. 5. The relationship between the three current models and the flowchart of the calculation for BDTT and fracture toughness.

3. Results

3.1. Validity of dislocation theory-based model

To verify the reasonableness of the BDT model, we calculate the BDTT of the TiVNbTa MPEAs. The experimental data is obtained from the existing TiVNbTa MPEAs (Scales et al., 2020). Table 1 shows the nominal chemical compositions of the TiVNbTa MPEAs. The fracture testing of the TiVNbTa MPEA is essential to measure the fracture toughness and BDTT. This testing is conducted over a range of temperatures to ensure its performance and prevent any potential catastrophic failures during service. By analyzing the fracture test and examining the fractography, the fracture toughness and the BDTT are obtained in Fig. 6, where the temperature of the four-point bending test is in the range of - 139 °C to 20 °C and the strain rate is 1×10^{-3} s⁻¹ (Scales et al., 2020). The fracture toughness versus temperature shows a soft BDT behavior (Fig. 6). The variation in fracture toughness with the temperature is observed in four distinct stages: brittle, semi-brittle, brittle-ductile transition, and ductile. When the temperature is low, the fracture toughness remains relatively stable at 43 MPa·m^{0.5}, but it increases to 65 MPa·m^{0.5} within the semi-brittle range. When the temperature is higher than -40 °C, the as-cast TiVNbTa MPEA exhibits high ductility and does not easily fracture. The soft transition phenomenon is a characteristic feature of semi-brittle BCC alloys, where the BDTT ranges from -47 °C to -27 °C in TiVNbTa MPEAs.

For the TiVNbTa MPEA, the related parameters are listed in Table 2. The full dislocation in the BCC crystal is $b = (\sqrt{3}/2)a_0$, the Poisson ratio is $\nu = 0.3$, and the half core width of the dislocation is $w_0 = 0.75a_0$. Thus, based on Table 2 and Eq. (10), the calculated BDTT of the TiVNbTa is $T_c = -39$ °C (Fig. 6), which is well in line with the experimental results (Scales et al., 2020). Then, the effects of component fluctuation, component randomness, and SRO on BDTT would be analyzed.

3.2. Effect of randomness and SRO on toughness

Based on the modified P-N model, the normalized dislocation friction stress is a statistical quantity with its own probability density distribution. Fig. 7 illustrates the normalized dislocation friction stress probability density function corresponding to different component randomness standard deviations and spatial correlation lengths. The average dislocation friction stress is calculated for different parameters, and the average dislocation friction stress is used as a description of the actual dislocation friction stress in MPEAs. Fig. 7a shows that the increasing standard deviation leads to a wide distribution of dislocation friction stress at a consistent spatial correlation length. This, in turn, leads to high average dislocation friction stress. Fig. 7b demonstrates that the increasing spatial correlation length at a fixed standard deviation leads to a wide distribution of dislocation friction stress and an increase in average dislocation friction stress.

Here, the variation of average dislocation friction stress with standard deviation and correlation length is presented in Fig. 8a. Here, when the standard deviation and correlation length is 0, it represents the pure metal; when the standard deviation and correlation length is small value, it represents the random alloys; when the standard deviation and correlation length is large value, it represents the MPEA with SRO. Fig. 8a shows the high dislocation friction stress in the MPEA compared to the pure metals (Pei et al., 2021; Xu et al., 2021), for the given standard deviation and correlation length. The increasing standard deviation at a fixed correlation length leads to the high dislocation friction stress. Furthermore, the increasing spatial correlation length and standard deviation both contribute to an increase in the dislocation friction stress, where these findings are confirmed in the previous work (Zhang et al., 2019a). Fig. 8b shows the distribution of BDTT for different component randomnesses and SRO degrees. Compared to the pure metals and random alloys, MPEA has a high BDTT. As the SRO degree increases, the BDTT rises (Tanaka et al., 2014). This trend would provide a way to control the BDTT for meeting the special service environment. Fig. 8c reveals the variation of fracture toughness at the BDTT in the MPEAs. As the spatial-correlation length and standard deviation increase, the fracture toughness of MPEAs is enhanced (Zhang et al., 2020). Fig. 8d reveals the variation of fracture toughness at room temperature in the MPEAs. As the spatial-correlation length and standard deviation increase, the fracture toughness in MPEAs.

To investigate the element distribution, the single crystal MPEA MoNbTaW sample is built using the large-scale molecular dynamics massively parallel simulator (LAMMPS) for Monte Carlo and molecular dynamics calculations. The MPEA sample with the size of $33.3 \times 3.1 \times 27.2 \, \mathrm{nm}^3$ has about 171,000 atoms. To construct the desired MPEA MoNbTaW sample containing the random elements, the atoms within the single crystal Mo structure are randomly substituted with atoms of Nb, Ta, and W, as presented in Fig. 9. The periodic boundary conditions are applied to all dimensions. The annealed MPEA samples are equilibrated using a hybrid Monte Carlo/molecular dynamics (MC/MD) approach (Fig. 9). In every MC step, a random atom is swapped with another random atom, following the Metropolis algorithm in the canonical ensemble. Each MC/MD step consists of 100 MC swaps followed by up to 10 MD relaxations. The system is maintained at a temperature of 300 K during these processes.

The Warren-Cowley (WC) parameter is widely utilized to describe the SRO degree in the MPEAs (Cowley, 1950), which is expressed as $\alpha_{ij}^N = \left(p_{ij}^N - C_j\right)/\left(\delta_{ij} - C_j\right)$. Here, N represents the Nth nearest-neighbor shell of the central atom i, α_{ij}^N is the WC parameter of i-j type

Table 1
The elemental content of the as-casted TiVNbTa MPEA.

Element	Ti	Та	Nb	V	O	С	N
at.%	23.592	26.797	25.041	24.439	0.0963	0.0276	0.0073

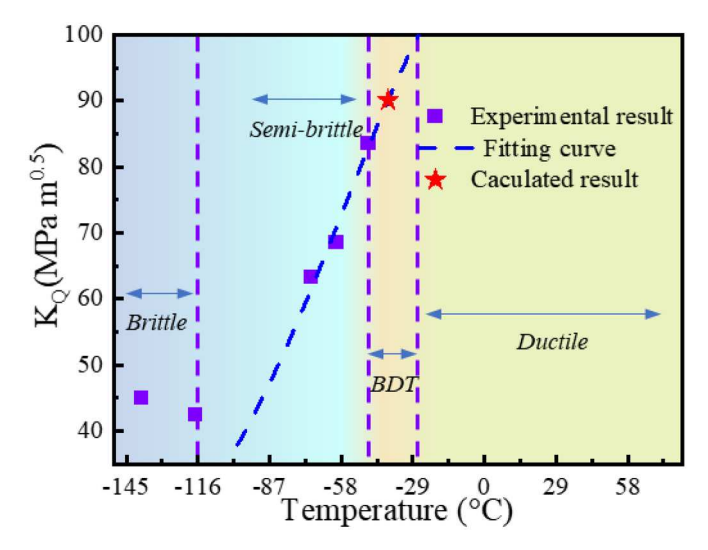


Fig. 6. The variation of the conditional fracture toughness in the TiVNbTa MPEA with the increasing temperature. The red five-pointed star represents the result of the model calculation.

 Table 2

 Parameters used in the BDTT calculations of TiVNbTa.

Parameters	Symbol	Magnitude
Yield strength (MPa)	$\sigma_{\rm y}$	1095
Lattice constant (nm)	a_0	3.237 (Scales et al., 2020)
Burgers vector (nm)	b	$\sqrt{3}a_0/2$
Shear modulus (GPa)	μ	49.5
Grain size (µm)	d	34.5 (Raman et al., 2021)
Distance to crack tip (µm)	1	0.1d(Zhang et al., 2019b)
Dislocation density (/cm ²)	ρ	10^{11}
Strain rate (/s)	$\dot{arepsilon}$	10^{-3} (Scales et al., 2020)
Specific surface energy (J/m ²)	γ_s	1 (Zhang et al., 2019b)
Vibration frequency of dislocation (/s)	ν_d	10^{13}
Boltzmann constant (J/K)	k	1.3806505×10^{-23}
Griffith crack size (cm)	c	2×10^{-4} (Zhang et al., 2019b
Coefficient	β	3

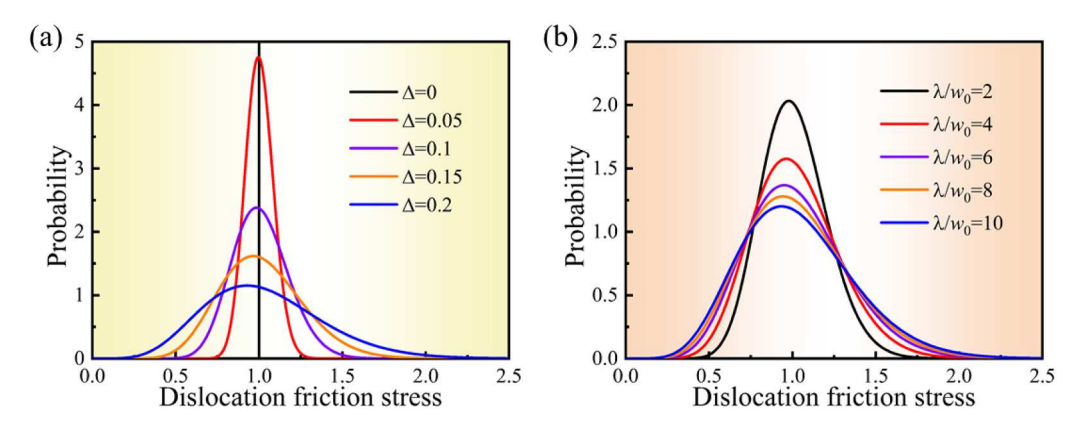


Fig. 7. (a) The normalized dislocation friction stress distribution versus the correlated random coefficient for several values of standard deviation at fixed spatial correlation length $\lambda/w_0=1$. (b) The normalized dislocation friction stress distribution versus the correlated random coefficient for some values of spatial correlation length at fixed standard deviation $\Delta=0.1$ (Zhang et al., 2019a).

atomic pair in the *N*th nearest-neighbor shell, C_j is the average concentration of element j in MPEAs, p_{ij}^N is the probability of locating a j-type atom within the *N*th nearest-neighbor shell of an i-type atom, and δ_{ij} is the Kronecker delta. The first-principles simulations show that the GSFE in the MPEAs with different SRO degrees follows a normal distribution (Ding et al., 2018). Here, the SRO parameters are

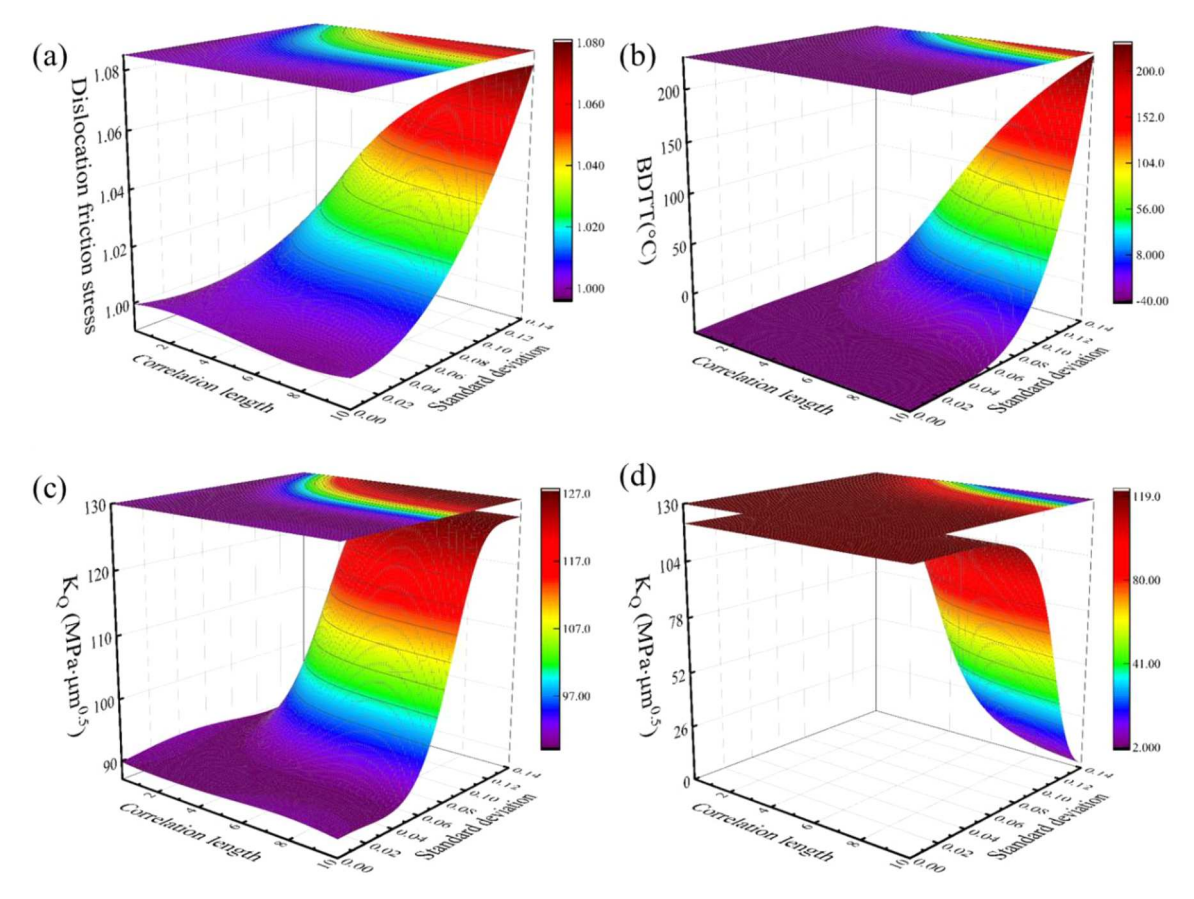


Fig. 8. (a) The normalized dislocation friction stress is a function of the component randomness and the short-range spatial correlation length in the TiVNbTa MPEA. (b) The effect of the component randomness and SRO spatial correlation length on BDTT. The effect of the component randomness and SRO spatial correlation length on the fracture toughness at the BDTT (c) and room temperature (d).

computed using the MD simulation in the BCC MoNbTaW MPEA (Fig. 10). The positive value of α_{w-w}^1 increases significantly in the MPEAs, indicating an increase in the degree of the local W segregation (Fig. 9).

The stacking fault energy curves of the random MPEA and SRO MPEA are presented in Fig. 11a-c, and the distributions of the corresponding two other elements are described in Fig. 11d. For different ID samples, the stable stacking fault energy shows significant fluctuations, which is $63.1 \pm 0.8 \text{ mJ/m}^2$ in the random MPEA and $78.4 \pm 1.1 \text{ mJ/m}^2$ in the SRO MPEA. By computing the SFE deviation under a given SRO MPEA, the corresponding correlation length can be obtained. For example, the short-range correlation length increases from 0.53 to 3.68 as the WC parameter increases from 0.18 to 0.24. Thus, when the correlation length is four times the dislocation core width and the standard deviation is 0.1, the BDTT is -22 °C in the MPEA TiVNbTa (Fig. 8). This comparison indicates that the atomic simulation results are consistent with the predicted results of the theoretical model, namely, the randomness to increase BDTT to a certain extent.

3.3. Effect of element on BDTT and fracture toughness

To assess the rationality and accuracy of the composition-dependent yield strength model, the predicted yield stress is compared to the result of experiment obtained from the BCC TiVNbTa MPEA. In the TiVNbTa MPEA, the Hall-Petch coefficient is taken as 592 MPa $\sqrt{\mu m}$ according to previous studies (Cordero et al., 2016; Raman et al., 2021). Table 3 presents the atomic radius and shear modulus of each element for the solid solution strengthening.

Fig. 12 shows the comparison of the yield strength from the theoretical model and experiment in TiVNbTa MPEAs. The yield strength predicted from the composition-dependent strength model is consistent with the experimental result (Lee et al., 2018). The yield strength of the TiVNbTa MPEA is composed of three components, namely solid solution strengthening caused by the severe lattice distortion, grain boundary strengthening, and dislocation strengthening. The yield strength experimentally obtained is 1273 MPa (Lee et al., 2018), and the result predicted from the composition-dependent yield strength model is 1095 MPa. The experimental and theoretical results deviate from each other by 14 %. Among these components, the solid solution strengthening contributes significantly, dominating the overall yield strength; the grain boundary strengthening is 100 MPa, which contributes the least to the yield strength; the dislocation strengthening is 443 MPa.

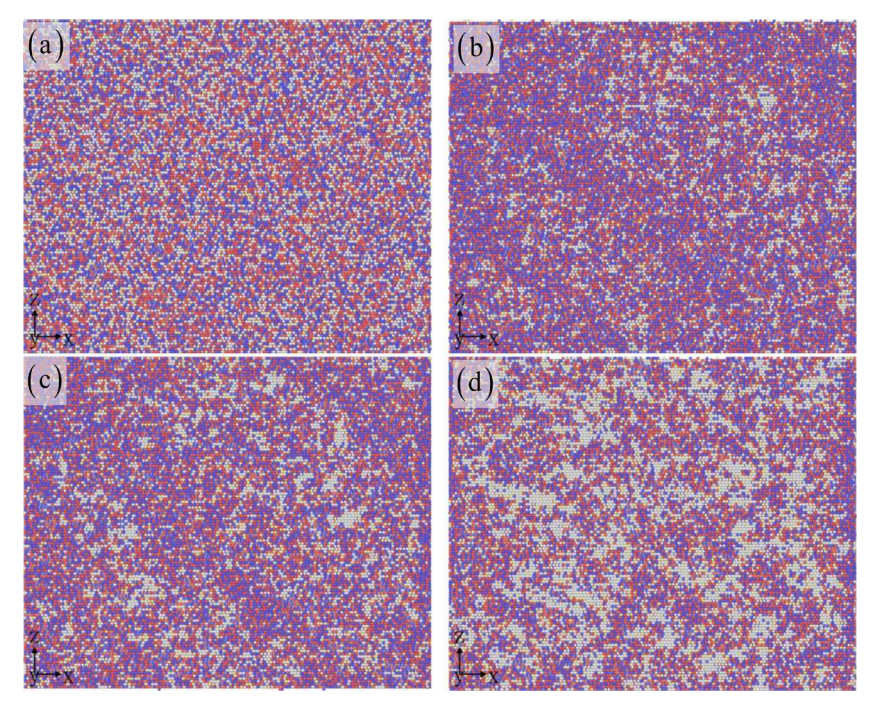


Fig. 9. The distribution of element in the samples with different MC cycle numbers: 0 (a), 20 (b), 50 (c), and 80 (d). <a> Mo, <a> Nb, <a> Ta, and <a> W.

The composition-dependent strength model is used to explore the effect of element concentration on the yield stress, atomic size mismatch, shear modulus mismatch, and solid solution strengthening in the BCC $Ti_xV_{50-x}NbTa$ MPEAs. Thus, the current model is utilized to predict the yield stress of the $Ti_xV_{50-x}NbTa$ MPEA when Ti element varies in the range of 15 % to 35 %. Fig. 13a demonstrates the calculated yield stress decreases with the increase Ti content in the $Ti_xV_{50-x}NbTa$ MPEAs. Figs. 13b, c depict the variations of the atomic radius mismatch and shear modulus mismatch with the increasing Ti content. At the given Ti concentration, the atomic radius mismatch of V element is larger than that of other elements, including Ti, Nb, and Ta. The atomic radii of other elements are very close to each other, while the atomic radius of V element is significantly smaller compared to the other elements (Li et al., 2020). The shear modulus mismatch of Ta element is higher than those of other elements, as exhibited in Fig. 13c. The shear moduli of the other elements are significantly smaller than that of the pure Ta. Fig. 13d shows the variation of solid solution strengthening due to the large atomic radius mismatch and shear modulus mismatch. From Figs. 13b-d, the V element to reduce the solid solution strengthening is the main reason for the decreasing yield strength of $Ti_xV_{50-x}NbTa$ MPEA. The atomic radius mismatch induces strong strengthening rather than the modulus mismatch, which agrees with the previous findings (Dou et al., 2024; Lee et al., 2018).

4. Discussion

Here, the impact of atomic radius and shear modulus from the other elements on the mechanical properties of MPEAs is evaluated

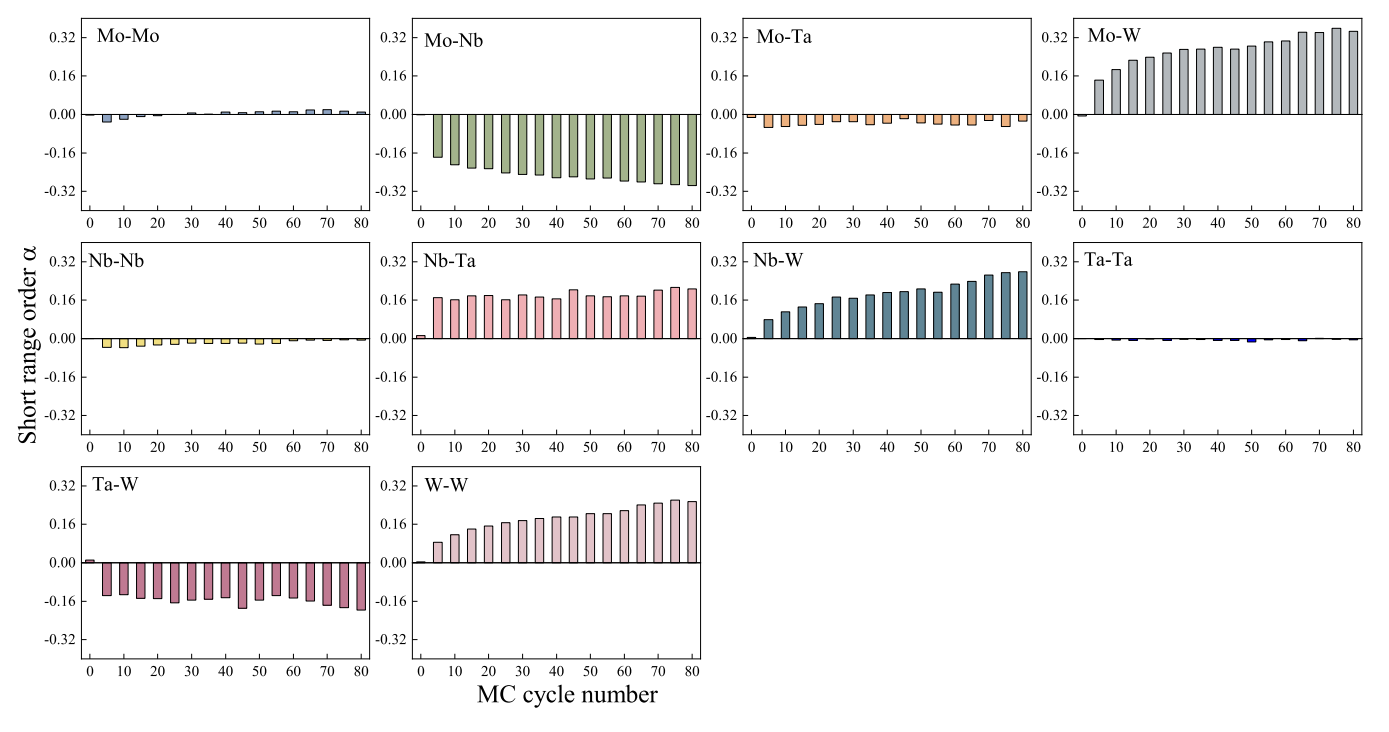


Fig. 10. Average SRO parameter obtained from MD simulation in the BCC MoNbTaW MPEA.

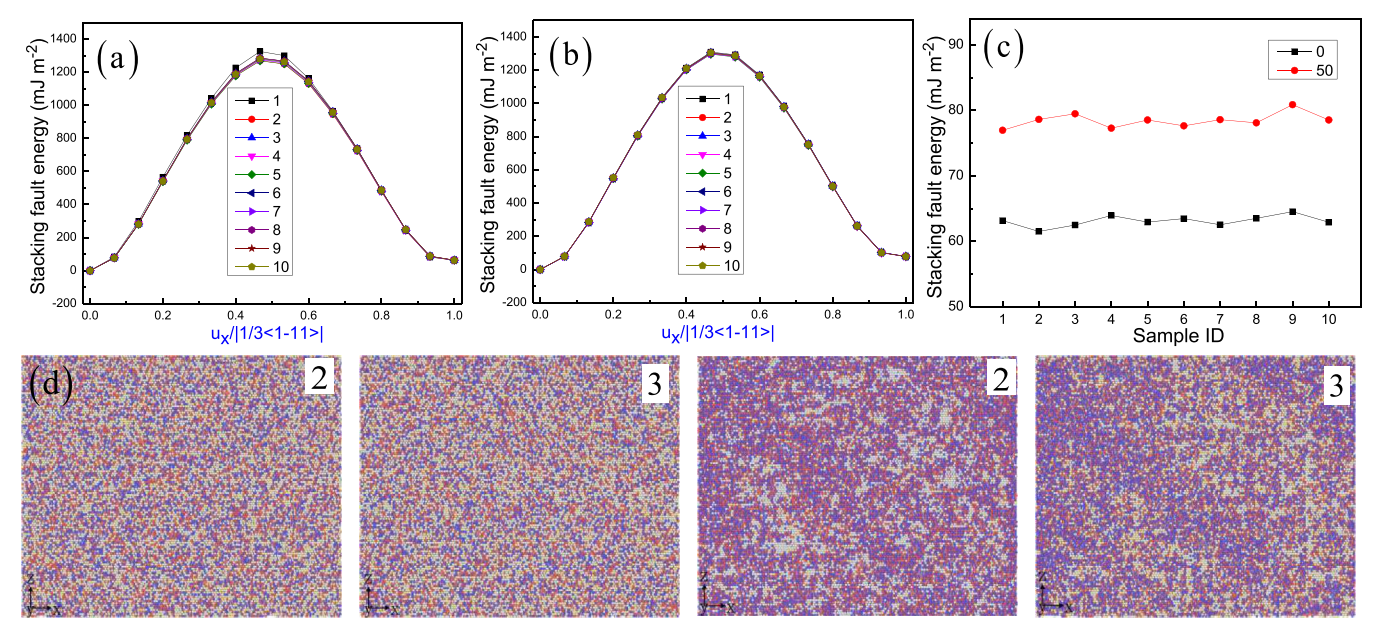


Fig. 11. The stacking fault energy in the random MPEA (a) and SRO MPEA (b), which contain the 10 independent samples at MC cycle number of 0 and 50. (c) The stable stacking fault energy for different samples. (d) The distribution of element in the sample ID: 2 and 3 at MC cycle number of 0 and 50.

Table 3
The atomic radius, shear modulus, and atomic fraction of Ti, V, Nb, and Ta.

Element	Ti	V	Nb	Та
Atomic radius, r (pm) Shear modulus, μ (GPa)	145 44	135 47	148 38	148 69
Atomic fraction, c (%)	25	25	25	25

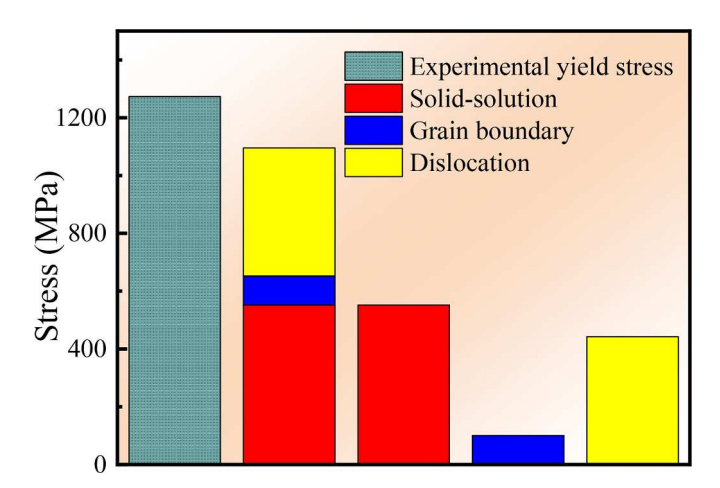


Fig. 12. Comparison of yield stress between the theoretical prediction and the experiment for the TiVNbTa MPEA. The grid columns correspond to the yield strength obtained from the experiment. The color column illustrates the contribution of various strengthening mechanisms to the yield strength of the TiVNbTa MPEA. The red column represents the solid solution strengthening, the blue column represents grain boundary strengthening, and the yellow column represents dislocation strengthening.

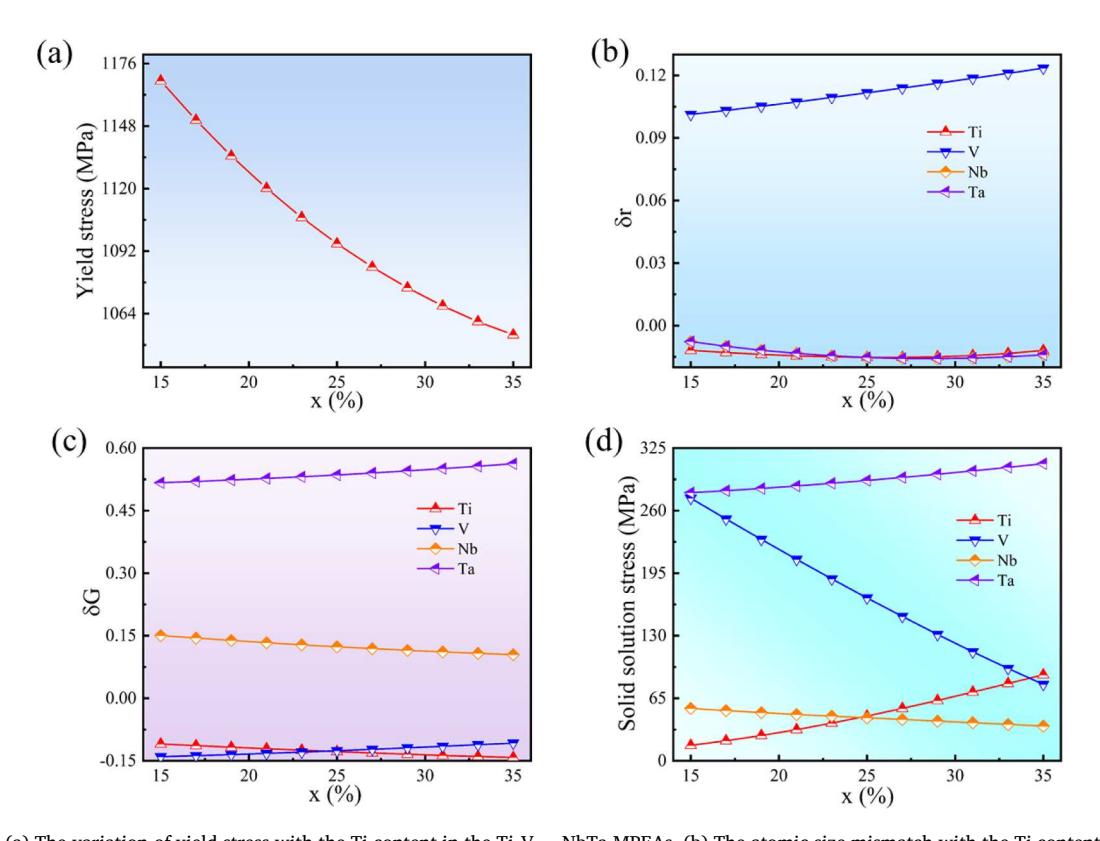


Fig. 13. (a) The variation of yield stress with the Ti content in the $Ti_xV_{50-x}NbTa$ MPEAs. (b) The atomic size mismatch with the Ti content. (c) The shear modulus mismatch with the Ti content. (d) Contribution of the Ti, V, Nb, and Ta to the solid solution strengthening.

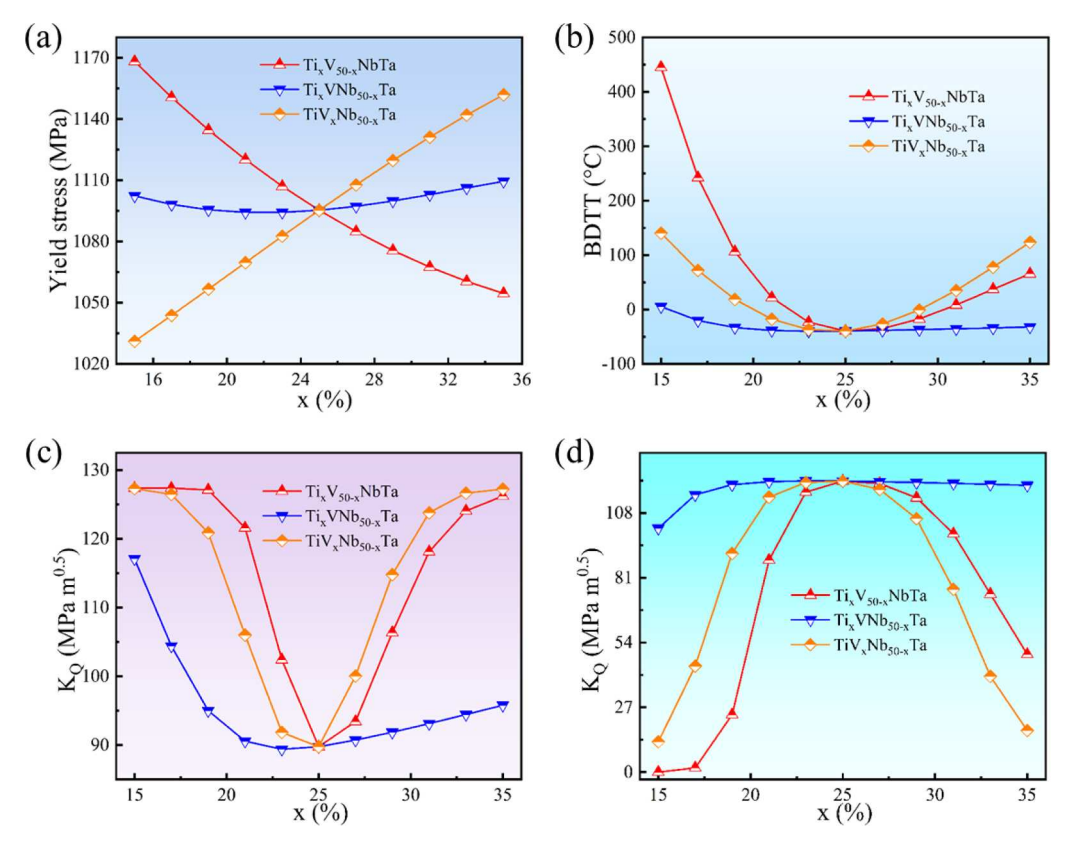


Fig. 14. (a) The variation of yield strength with the elemental concentration in the $Ti_xV_{50-x}NbTa$, $Ti_xVNb_{50-x}Ta$ and $TiV_xNb_{50-x}Ta$ MPEAs. (b) The relationship between BDTT and elemental content. (c) The correlation between the fracture toughness and elemental content at the BDTT. (d) The correlation between the fracture toughness and elemental content at room temperature.

for a constant composition content. In fact, based on the lattice distortion related strengthening model, the effects of atomic radius and shear modulus on the yield strength, BDTT, and fracture toughness are quantitatively evaluated in the TiVNbTa MPEA. For example, the other elements (denoted as X) can form VNbTaX, TiVTaX, and TiVNbX MPEAs. Then, the influence of the atomic radius and shear modulus on the mechanical properties is quantitatively assessed in VNbTaX, TiVTaX, and TiVNbX MPEAs. In Fig. 15a, when the element radius is less than 148pm, the yield strength improves with the increase atomic radius in the VNbTaX, TiVTaX, and TiVNbX MPEAs. It is evident that the VNbTaX MPEA has the high strength. As shown in Fig. 15b, the BDTT decreases in both TiVTaX and TiVNbX MPEA, as the atomic radius increases. However, the BDTT for VNbTaX is intricate, and it shows a complex relationship with the increasing atomic radius. This trend shows a pattern of initially decreasing, then increasing, and ultimately decreasing. Fig. 15c shows that the fracture toughness at the BDTT initially decreases, and then increases with the increasing atomic radius in VNbTaX. Similarly, the fracture toughness of TiVTaX and TiVNbX follows a similar trend as the atomic radius increases. Here, the other elements lead to the improved strength and fracture toughness in VNbTaX. Fig. 15d shows that the trend of fracture toughness in relation to atomic radius is almost the same at room temperature for TiVTaX and TiVNbX. It is worth noting that the MPEAs exhibit a high fracture toughness for the large atomic radius at room temperature.

Fig. 16 presents the effect of shear modulus of the other elements on the yield stress, BDTT, and fracture toughness in the MPEAs. From Fig. 16a, as the shear modulus increases, the yield strength of VNbTaX exhibits a parabolic trend, while TiNbTaX and TiVTaX show similar trends. By substituting Zr for Nb, experimental results reveal that the hardness of TiVZrTa surpasses that of TiVNbTa (Kareer et al., 2019). This enhancement in hardness also signifies a corresponding increase in the strength. TiNbTaX MPEA exhibits superior yield strength under the condition that the atomic radius of the other element remains constant and the shear modulus is below 45 GPa. In Fig. 16b, the BDTT of TiNbTaX exhibits a more pronounced variation in response to the shear modulus change. When the shear modulus is below 45 GPa, VNbTaX exhibits a low BDTT. Fig. 16c shows that the trends of fracture toughness at the BDTT in relation to shear modulus for VNbTaX and TiVTaX are quite similar. However, it is worth noting that TiNbTaX exhibits a notably high level of fracture toughness when the shear modulus is below 45 GPa. Fig. 16d shows that the trends of fracture toughness at room temperature in relation to shear modulus for VNbTaX and TiVTaX are quite similar. However, it is worth noting that VNbTaX exhibits a notably high level of toughness when the shear modulus is below 45 GPa.

Fig. 17 illustrates the brittle/ductile characteristic distribution of TiVNbTa MPEA at different temperatures. When the given temperature is $T_1 = -39$ °C, the microstructural parameters including standard deviation and spatial correlation length fall within the blue shaded region, indicating that the material is ductile; when the given temperature is $T_2 = -15$ °C, the microstructural parameters

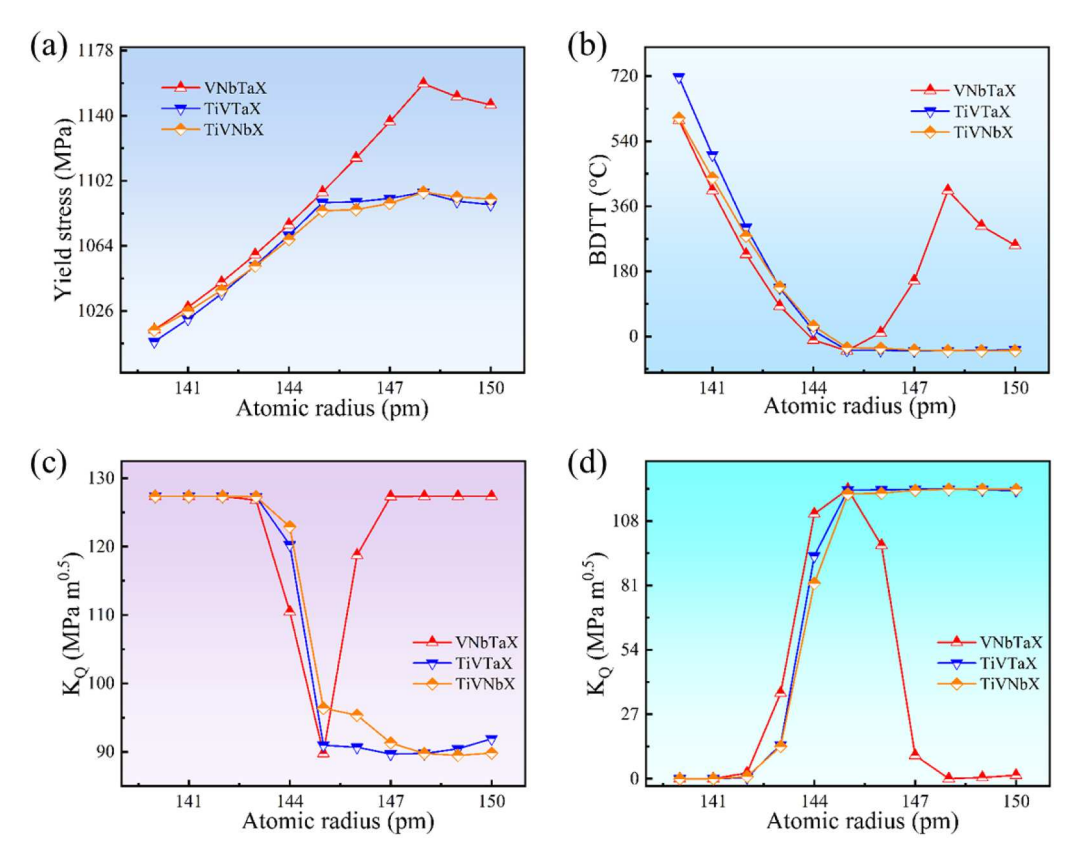


Fig. 15. The variation of (a) yield strength, and (b) BDTT for different atomic radii. The relationship between atomic radius and fracture toughness at the BDTT (c) and room temperature (d). X represents the other element.

fall within the yellow shaded region, indicating that the material exhibits brittle properties. Based on the microstructure-based BDT criterion, it is possible to analyze the conditions satisfied by the microstructural parameters of the MPEAs in order to maintain ductility at a given temperature. Thus, such results provide the opportunity to adjust the mechanical properties through alterations in the microstructure. It is anticipated that this work would aid in the prediction of the BDTT and fracture toughness of MPEAs, and developing materials for extreme working conditions.

5. Conclusions

In the current work, a dislocation theory-based model coupling the critical energy model, the modified lattice friction stress model, and the composition-dependent strength model is developed to predict the BDTT and fracture toughness in MPEAs. The yield stress of TiVNbTa predicted by the composition-dependent strength model shows good agreement with the experimental results. Furthermore, the analytical model accurately predicts the BDTT in the TiVNbTa MPEA, consistent with previous experimental observations. The impact of standard deviation, short-range spatial correlation length, elemental concentration fluctuation, and element substitution on the toughness is investigated in the TiVNbTa MPEA. A high degree of short-range spatial correlation length increases dislocation friction stress, but it does not necessarily reduce the BDTT in TiVNbTa. The solid-solution strengthening is identified as the main mechanism for strengthening in TiVNbTa. In the Ti-V-Nb-Ta MPEAs, the ductility of $\text{Ti}_x\text{VNb}_{50-x}\text{Ta}$ is most affected by changes in concentration. A microstructure-based BDT criterion for predicting the necessary microstructural parameters for MPEA is proposed to exhibit ductility at a specific temperature. These findings support the use of the developed methods for computationally guided design of advanced BCC MPEAs with superior strength and toughness.

CRediT authorship contribution statement

Zebin Han: Writing – original draft, Visualization, Validation, Software, Resources, Methodology, Investigation, Formal analysis, Data curation. **Bin Liu:** Writing – original draft, Supervision, Methodology, Investigation, Funding acquisition, Formal analysis, Data

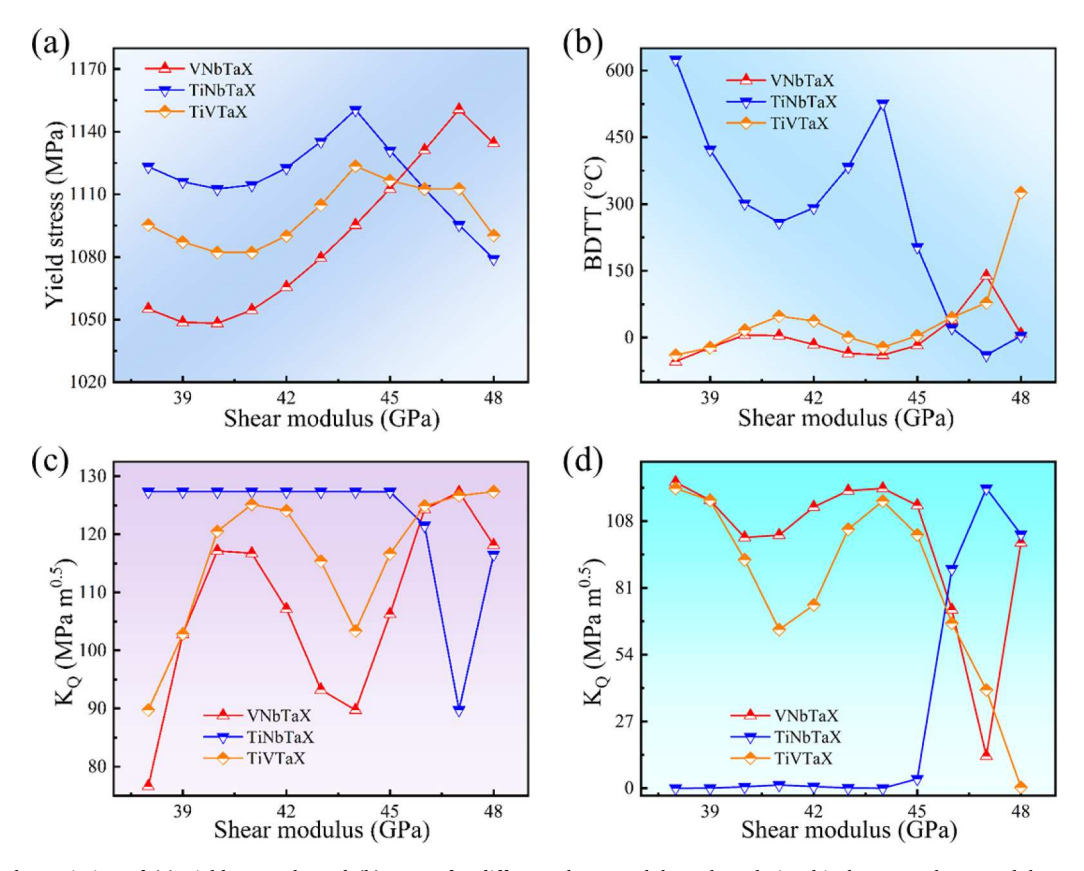


Fig. 16. The variation of (a) yield strength, and (b) BDTT for different shear modulus. The relationship between shear modulus and fracture toughness at the BDTT (c) and room temperature (d). X represents the other element.

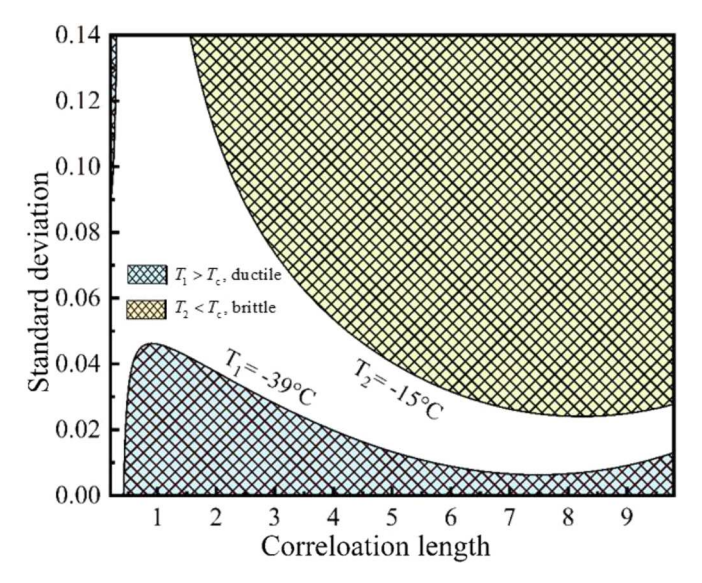


Fig. 17. The distribution of brittle and ductile characteristics at a given temperature $T_1 = -39$ °C and $T_2 = -15$ °C in the BCC TiVNbTa MPEA.

curation. **Qihong Fang:** Writing – original draft, Validation, Supervision, Methodology, Investigation, Funding acquisition. **Peter K Liaw:** Writing – original draft, Supervision, Methodology, Investigation, Funding acquisition. **Jia Li:** Writing – original draft, Software, Methodology, Investigation, Funding acquisition, Conceptualization.

Declaration of competing interest

The authors declare that they have no known competing financial interests or personal relationships that could have appeared to influence the work reported in this paper.

Data Availability

Data will be made available on request.

Acknowledgement

The present was supported by the National Natural Science Foundation of China (U2267252, 12372069, and 12172123), Natural Science Foundation of Hunan Province (2022JJ20001), and the Hunan Provincial Innovation Foundation for Postgraduate (CX20220378). PKL very much appreciates the support from (1) the National Science Foundation (DMR – 1611180, 1809640, and 2226508) and (2) the US Army Research Office (W911NF-13–1–0438 and W911NF-19–2–0049).

Appendix A

In MPEA, available information suggests that normal, gamma, and Weibull distributions can be used to characterize the statistical distribution of the interplaner potential perturbation. Therefore, the probability density distribution of the dislocation friction stress is calculated under these three distributions.

For a normal distribution, the probability density function is expressed as

$$P_{\omega}(u;1,\Delta) = \frac{1}{\Delta\sqrt{2\pi}}e^{-\frac{(u-1)^2}{2\Delta^2}} \tag{A.1}$$

The average and standard deviation of the other two distributions are the same as those of the normal distribution. The probability density function of gamma distribution is

$$P_{\omega}(u;k,\theta) = 1/\left(\Gamma(k)\theta^{k}\right)u^{k-1}e^{-u/\theta} \tag{A.2}$$

here, θ and k are parameters of the gamma distribution. $\Gamma(k)$ is gamma function. In order to make the gamma distribution have an average value of 1 and a standard deviation of Δ , we set $\theta = \Delta^2$ and $k = 1/\Delta^2$.

The probability density function of the Weibull distribution is expressed as

$$f(u; p, q) = \frac{q}{p} \left(\frac{u}{p}\right)^{q-1} e^{-(u/p)^{q}}$$
(A.3)

where p is scale parameter, q is shape parameter.

The results obtained using these distributions are compared (Fig. A1). It can be seen that the results using normally distributed dislocation friction stress approximate well the results of the gamma distribution. Whereas the results calculated from the Weibull distribution are not consistent with the properties in MPEA. Therefore, the normal distribution is chosen for the study due to its flexibility and rationality.

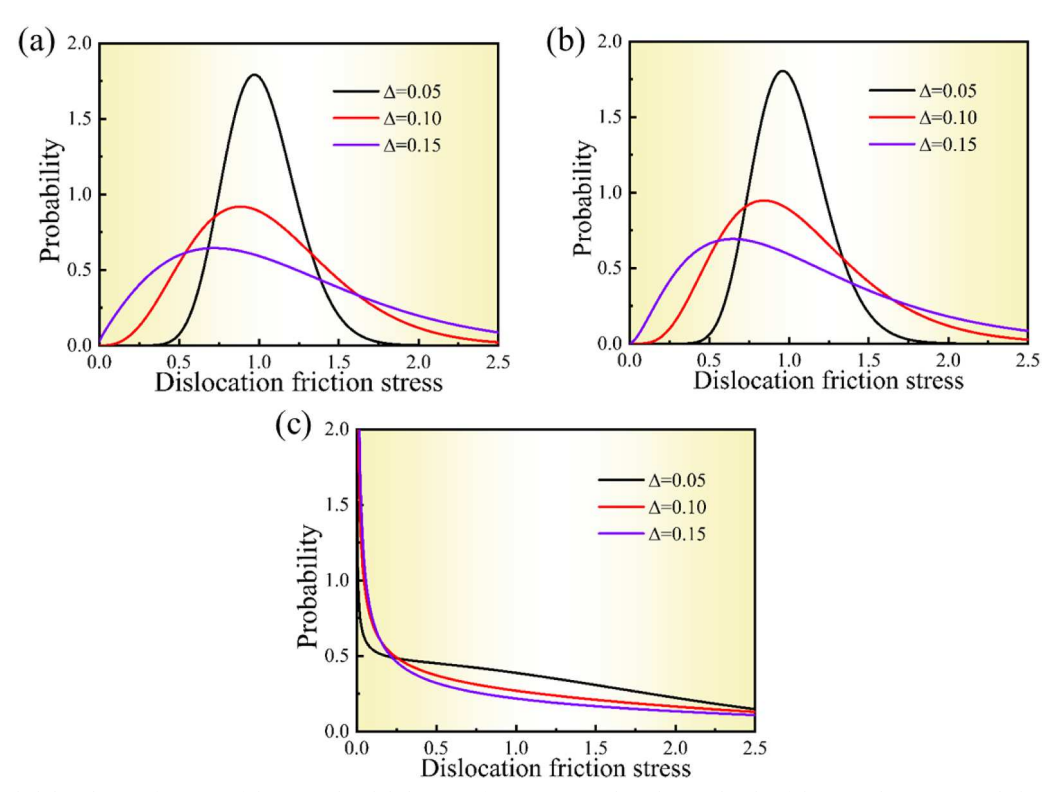


Fig. A1. Probability density function of the normalized dislocation friction stress when the amplitude of the interplanar potential obeys (a) normal distribution, (b) gamma distribution, and (c) Weibull distribution.

References

Abu-Odeh, A., Asta, M., 2022. Modeling the effect of short-range order on cross-slip in an FCC solid solution. Acta Mater 226, 117615.

Alkan, S., Ojha, A., Sehitoglu, H., 2018. Determination of latent hardening response for FeNiCoCrMn for twin-twin interactions. Acta Mater 147, 149-164. An, Z., Mao, S., Yang, T., Liu, C.T., Zhang, B., Ma, E., Zhou, H., Zhang, Z., Wang, L., Han, X., 2021. Spinodal-modulated solid solution delivers a strong and ductile refractory high-entropy alloy. Mater. Horiz. 8, 948-955.

Anderson, P.M., Hirth, J.P., Lothe, J., 2017. Theory of Dislocations. Cambridge University Press.

Argon, A., 2007. Strengthening Mechanisms in Crystal Plasticity. OUP, Oxford.

Belcher, C.H., MacDonald, B.E., Apelian, D., Lavernia, E.J., 2023. The role of interstitial constituents in refractory complex concentrated alloys. Prog. Mater. Sci., 101140

Bonnekoh, C., Jäntsch, U., Hoffmann, J., Leiste, H., Hartmaier, A., Weygand, D., Hoffmann, A., Reiser, J., 2019. The brittle-to-ductile transition in cold rolled tungsten plates: impact of crystallographic texture, grain size and dislocation density on the transition temperature. Int. J. Refract. Met. H. 78, 146-163.

Cantor, B., Chang, I.T.H., Knight, P., Vincent, A.J.B., 2004. Microstructural development in equiatomic multicomponent alloys. Mater. Sci. Eng., A 375, 213–218. Chen, L., Liu, W., Yu, L., Cheng, Y., Ren, K., Sui, H., Yi, X., Duan, H., 2020. Probabilistic and constitutive models for ductile-to-brittle transition in steels: a competition between cleavage and ductile fracture. J. Mech. Phys. Solids 135, 103809.

Chen, S., Aitken, Z.H., Pattamatta, S., Wu, Z., Yu, Z.G., Srolovitz, D.J., Liaw, P.K., Zhang, Y.W., 2021a. Simultaneously enhancing the ultimate strength and ductility of high-entropy alloys via short-range ordering. Nat. Commun. 12, 4953.

Chen, X., Wang, Q., Cheng, Z., Zhu, M., Zhou, H., Jiang, P., Zhou, L., Xue, Q., Yuan, F., Zhu, J., Wu, X., Ma, E., 2021b. Direct observation of chemical short-range order in a medium-entropy alloy. Nature 592, 712-716.

Chen, Y., Feng, H., Li, J., Liu, B., Jiang, C., Liu, Y., Fang, Q., Liaw, P.K., 2024. Dislocation flow turbulence simultaneously enhances strength and ductility. Proc. Natl. Acad. Sci. USA 121, e2316912121.

Cordero, Z.C., Knight, B.E., Schuh, C.A., 2016. Six decades of the Hall-Petch effect - a survey of grain-size strengthening studies on pure metals. Int. Mater. Rev. 61,

495-512

Courtney, T.H., 2005. Mechanical Behavior of Materials. Waveland Press.

Cowley, J.M., 1950. An approximate theory of order in alloys. Phys. Rev. 77, 669-675.

Cui, Y., Po, G., Ghoniem, N., 2016. Controlling strain bursts and avalanches at the nano- to micrometer scale. Phys. Rev. Lett. 117, 155502.

Cui, Y., Po, G., Srivastava, P., Jiang, K., Gupta, V., Ghoniem, N., 2020. The role of slow screw dislocations in controlling fast strain avalanche dynamics in bodycentered cubic metals. Int. J. Plast. 124, 117-132.

Cui, Y., Wang, T., Luo, S., Li, Z., Li, Z., 2022. A discrete-continuous model of three-dimensional dislocation elastodynamics. Int. J. Plast. 152, 103221.

Ding, J., Yu, O., Asta, M., Ritchie, R.O., 2018. Tunable stacking fault energies by tailoring local chemical order in CrCoNi medium-entropy alloys. Proc. Natl. Acad. Sci. USA 115, 8919-8924.

Dou, B., Cui, J., Guo, R., Liu, S., Zhang, T., Chen, S., Li, B., Wang, X., Wang, B., Sun, S., Wang, L., Xue, Y., 2024. Modulus-mismatch strategy optimized lightweight refractory high-entropy alloys for superior synergy of mechanical properties and thermostability. Mater. Sci. Eng., A 908, 146767.

Fan, H., Wang, Q., El-Awady, J.A., Raabe, D., Zaiser, M., 2021. Strain rate dependency of dislocation plasticity. Nat. Commun. 12, 1845.

Fang, Q., Huang, Z., Li, L., Huang, Z., Liu, B., Liu, Y., Li, J., Liaw, P.K., 2022. Modeling the competition between solid solution and precipitate strengthening of alloys in a 3D space. Int. J. Plast. 149, 103152.

- George, E.P., Raabe, D., Ritchie, R.O., 2019. High-entropy alloys. Nat. Rev. Mater. 4, 515-534.
- Guo, Z., Song, Z., Liu, H., Hu, D., Huang, D., Yan, X., Yan, W., 2024. A dislocation-based damage-coupled constitutive model for single crystal superalloy: unveiling the effect of secondary orientation on creep life of circular hole. Int. J. Plast. 173, 103874.
- Heslop, J., Petch, N.J., 1956. The stress to move a free dislocation in alpha iron. Philos. Mag. 1, 866-873.
- Heslop, J., Petch, N.J., 1958. The ductile-brittle transition in the fracture of α-iron: II. Philos. Mag. 3, 1128–1136.
- Hirsch, P.B., Roberts, S.G., 1996. Comment on the brittle-to-ductile transition: a cooperative dislocation generation instability; dislocation dynamics and the strain-rate dependence of the transition temperature. Acta Mater 44, 2361–2371.
- Hirsch, P.B., Roberts, S.G., Samuels, J., 1989. The brittle-ductile transition in silicon. II. Interpretation. Proc. R. Soc. Lond. A Math. Phys. Sci. 421, 25–53.
- Hirth, J.P., Lothe, J., Mura, T., 1983. Theory of dislocations. J. Appl. Mech. 50, 476-477.
- Hu, Y.J., Sundar, A., Ogata, S., Qi, L., 2021. Screening of generalized stacking fault energies, surface energies and intrinsic ductile potency of refractory multicomponent alloys. Acta Mater 210, 116800.
- Huang, W., Wang, X., Qiao, J., Wu, Y., 2022. Microstructures and mechanical properties of TiZrHfNbTaWx refractory high entropy alloys. J. Alloys Compd. 914, 165187.
- Jian, W., Ren, L., 2024. Insights into orientation-dependent plasticity deformation of HfNbTaTiZr refractory high entropy alloy: an atomistic investigation. Int. J. Plast. 173, 103867.
- Jouiad, M., Pettinari, F., Clément, N., Coujou, A., 1999. Dynamic friction stresses in the γ phase of a nickel-based superalloy. Philos. Mag. A 79, 2591–2602.
- Kareer, A., Waite, J.C., Li, B., Couet, A., Armstrong, D.E.J., Wilkinson, A.J., 2019. Low activation, refractory, high entropy alloys for nuclear applications. J. Nucl. Mater. 526, 151744.
- Kim, Y.K., Choe, J., Lee, K.A., 2019. Selective laser melted equiatomic CoCrFeMnNi high-entropy alloy: microstructure, anisotropic mechanical response, and multiple strengthening mechanism. J. Alloys Compd. 805, 680–691.
- Körmann, F., Ruban, A.V., Sluiter, M.H., 2017. Long-ranged interactions in bcc NbMoTaW high-entropy alloys. Mater. Res. Lett. 5, 35-40.
- Krasnikov, V.S., Mayer, A.E., 2018. Influence of local stresses on motion of edge dislocation in aluminum. Int. J. Plast. 101, 170-187.
- Labusch, R., 1970. A statistical theory of solid solution hardening, Physica Status Solidi (b) 41, 659-669.

Lawn, B., 1993. Fracture of brittle solids, 194.

- Lee, C., Song, G., Gao, M.C., Feng, R., Chen, P., Brechtl, J., Chen, Y., An, K., Guo, W., Poplawsky, J.D., Li, S., Samaei, A.T., Chen, W., Hu, A., Choo, H., Liaw, P.K., 2018. Lattice distortion in a strong and ductile refractory high-entropy alloy. Acta Mater 160, 158–172.
- Li, J., Chen, Y., He, Q., Xu, X., Wang, H., Jiang, C., Liu, B., Fang, Q., Liu, Y., Yang, Y., Liaw, P.K., Liu, C.T., 2022a. Heterogeneous lattice strain strengthening in severely distorted crystalline solids. Proc. Natl. Acad. Sci. USA 119, e2200607119.
- Li, J., Fang, Q., Liaw, P.K., 2021a. Microstructures and properties of high-entropy materials: modeling, simulation, and experiments. Adv. Eng. Mater. 23, 2001044. Li, J., Ren, S., Liu, B., Liaw, P.K., Fang, Q., 2023a. Influence of chemistry and temperature on mechanical behavior and deformation mechanisms of refractory high-entropy alloys: an integrated simulation-modeling analysis. Acta Mech. Sin. 40, 423122.
- Li, L., Fang, Q., Li, J., Liu, B., Liu, Y., Liaw, P.K., 2020. Lattice-distortion dependent yield strength in high entropy alloys. Mater. Sci. Eng., A 784, 139323.
- Li, Q.J., Sheng, H., Ma, E., 2019. Strengthening in multi-principal element alloys with local-chemical-order roughened dislocation pathways. Nat. Commun. 10, 3563.
- Li, W., Chen, S., Aitken, Z., Zhang, Y.W., 2023b. Shock-induced deformation and spallation in CoCrFeMnNi high-entropy alloys at high strain-rates. Int. J. Plast. 168, 103691.
- Li, Z., Liu, Z., Zhuang, Z., Cui, Y., 2021b. Temperature dependent deformation localization in irradiated tungsten. Int. J. Plast. 146, 103077.
- Li, Z., Ma, S., Zhao, S., Zhaog, W., Peng, F., Li, Q., Yang, T., Wu, C.Y., Wei, D., Chou, Y.C., Liaw, P.K., Gao, Y., Wu, Z., 2023c. Achieving superb strength in single-phase FCC alloys via maximizing volume misfit. Mater. Today 63, 108–119.
- Li, Z.J., Wang, T., Chu, D.Y., Liu, Z.L., Cui, Y.N., 2022b. A coupled crystal-plasticity and phase-field model for understanding fracture behaviors of single crystal tungsten. Int. J. Plast. 157, 103375.
- Liu, W.H., Wu, Y., He, J.Y., Nieh, T.G., Lu, Z.P., 2013. Grain growth and the Hall–Petch relationship in a high-entropy FeCrNiCoMn alloy. Scr. Mater. 68, 526–529. Lu, Y., Zhang, Y.H., Ma, E., Han, W.Z., 2021. Relative mobility of screw versus edge dislocations controls the ductile-to-brittle transition in metals. Proc. Natl. Acad. Sci. USA 118, e2110596118.
- Mak, E., Yin, B., Curtin, W.A., 2021. A ductility criterion for bcc high entropy alloys. J. Mech. Phys. Solids 152, 104389.
- Miracle, D.B., Senkov, O.N., 2017. A critical review of high entropy alloys and related concepts. Acta Mater 122, 448-511.
- Nabarro, F., 1947. Dislocations in a simple cubic lattice. Proc. Phys. Soc. 59, 256.
- Pei, Z., Zhang, S., Lei, Y., Zhang, F., Chen, M., 2021. Decoupling between Shockley partials and stacking faults strengthens multiprincipal element alloys. Proc. Natl. Acad. Sci. USA 118, e2114167118.
- Peierls, R., 1940. The size of a dislocation. Proc. Phys. Soc. 52, 34.
- Petch, N.J., 1958. The ductile-brittle transition in the fracture of α -iron: I. Philos. Mag. 3, 1089–1097.
- Pettinari-Sturmel, F., Jouiad, M., Kirchner, H.O.K., Clément, N., Coujou, A., 2002. Local disordering and reordering phenomena induced by mobile dislocations in short-range-ordered solid solutions. Philos. Mag. A 82, 3045–3054.
- Raman, L., Anupam, A., Karthick, G., Berndt, C.C., Ang, A.S.M., Narayana Murty, S.V.S., Fabijanic, D., Murty, B.S., Kottada, R.S., 2021. Strengthening mechanisms in CrMoNbTiW refractory high entropy alloy. Mater. Sci. Eng., A 819, 141503.
- Rao, Y., Baruffi, C., De Luca, A., Leinenbach, C., Curtin, W.A., 2022. Theory-guided design of high-strength, high-melting point, ductile, low-density, single-phase BCC high entropy alloys. Acta Mater 237, 118132.
- Sailors, R.H., Corten, H.T., 1972. Relationship between material fracture toughness using fracture mechanics and transition temperature tests, fracture toughness: Part II. ASTM International.
- Santodonato, L.J., Zhang, Y., Feygenson, M., Parish, C.M., Gao, M.C., Weber, R.J., Neuefeind, J.C., Tang, Z., Liaw, P.K., 2015. Deviation from high-entropy configurations in the atomic distributions of a multi-principal-element alloy. Nat. Commun. 6, 5964.
- Scales, R.J., Armstrong, D.E., Wilkinson, A.J., Li, B.S., 2020. On the brittle-to-ductile transition of the as-cast TiVNbTa refractory high-entropy alloy. Mater 14, 100940.
- Schön, C.G., 2021. On short-range order strengthening and its role in high-entropy alloys. Scr. Mater. 196, 113754.
- Senkov, O.N., Miller, J.D., Miracle, D.B., Woodward, C., 2015. Accelerated exploration of multi-principal element alloys with solid solution phases. Nat. Commun. 6, 6520
- Senkov, O.N., Miracle, D.B., Chaput, K.J., Couzinie, J.P., 2018. Development and exploration of refractory high entropy alloys—A review. J. Mater. Res. 33, 3092–3128.
- Senkov, O.N., Senkova, S.V., Woodward, C.J.A.M., 2014. Effect of aluminum on the microstructure and properties of two refractory high-entropy alloys. Acta Mater 68, 214–228.
- Senkov, O.N., Wilks, G.B., Miracle, D.B., Chuang, C.P., Liaw, P.K., 2010. Refractory high-entropy alloys. Intermetallics 18, 1758–1765.
- Shen, F., Sparrer, Y., Rao, J., Könemann, M., Münstermann, S., Lian, J., 2024. A forming limit framework accounting for various failure mechanisms: localization, ductile and cleavage fracture. Int. J. Plast., 103921
- Singh, P., Smirnov, A.V., Johnson, D.D., 2015. Atomic short-range order and incipient long-range order in high-entropy alloys. Phys. Rev. B 91, 224204.
- Singh, P., Vela, B., Ouyang, G., Argibay, N., Cui, J., Arroyave, R., Johnson, D.D., 2023. A ductility metric for refractory-based multi-principal-element alloys. Acta Mater 257, 119104.
- Soler, R., Evirgen, A., Yao, M., Kirchlechner, C., Stein, F., Feuerbacher, M., Raabe, D., Dehm, G., 2018. Microstructural and mechanical characterization of an equiatomic YGdTbDyHo high entropy alloy with hexagonal close-packed structure. Acta Mater 156, 86–96.
- Suzuki, K., Koyama, M., Hamada, S., Tsuzaki, K., Noguchi, H., 2020. Planar slip-driven fatigue crack initiation and propagation in an equiatomic CrMnFeCoNi high-entropy alloy. Int. J. Fatigue 133, 105418.

Tamm, A., Aabloo, A., Klintenberg, M., Stocks, M., Caro, A., 2015. Atomic-scale properties of Ni-based FCC ternary, and quaternary alloys. Acta Mater 99, 307–312. Tanaka, M., Onomoto, T., Furusho, C., Tsuchiyama, T., Higashida, K., 2014. Decrease in the brittle-to-ductile transition temperature in Cu added Nickel-free austenitic stainless steels. ISIJ Int 54, 1735–1740.

Tanaka, M., Onomoto, T., Tsuchiyama, T., Higashida, K., 2012. Brittle-to-ductile transition in Nickel-free austenitic stainless steels with high nitrogen. ISIJ Int 52, 915–921

Tanaka, M., Tarleton, E., Roberts, S.G., 2008. The brittle-ductile transition in single-crystal iron. Acta Mater 56, 5123-5129.

Toda-Caraballo, I., Rivera-Díaz-del-Castillo, P.E., 2015. Modelling solid solution hardening in high entropy alloys. Acta Mater 85, 14-23.

Vegard, L., 1916. VI. Results of crystal analysis. Lond. Edinb. Dubl. Phil. Mag. 32, 65-96.

Wang, M., Ma, Z., Xu, Z., Cheng, X., 2021. Effects of vanadium concentration on mechanical properties of VxNbMoTa refractory high-entropy alloys. Mater. Sci. Eng., A 808, 140848.

Wu, Y., Zhang, F., Yuan, X., Huang, H., Wen, X., Wang, Y., Zhang, M., Wu, H., Liu, X., Wang, H., Jiang, S., Lu, Z., 2021. Short-range ordering and its effects on mechanical properties of high-entropy allows. J. Mater. Sci. Tech. 62, 214–220.

Xu, S., Su, Y., Jian, W.R., Beyerlein, I.J., 2021. Local slip resistances in equal-molar MoNbTi multi-principal element alloy. Acta Mater 202, 68–79.

Yang, T., Zhao, Y., Li, W., Yu, C., Luan, J., Lin, D., Fan, L., Jiao, Z., Liu, W., Liu, X., Kai, J., Huang, J., liu, C., 2020. Ultrahigh-strength and ductile superlattice alloys with nanoscale disordered interfaces. Science 369, 427–432.

Ye, Y.F., Wang, Q., Lu, J., Liu, C.T., Yang, Y., 2016. High-entropy alloy: challenges and prospects. Mater. Today 19, 349-362.

Yeh, J.W., Chen, S.K., Lin, S.J., Gan, J.Y., Chin, T.S., Shun, T.T., Tsau, C.H., Chang, S.Y., 2004. Nanostructured high-entropy alloys with multiple principal elements: novel alloy design concepts and outcomes. Adv. Eng. Mater. 6, 299–303.

You, T., Waisman, H., Zhu, Q.Z., 2021. Brittle-ductile failure transition in geomaterials modeled by a modified phase-field method with a varying damage-driving energy coefficient. Int. J. Plast. 136, 102836.

Zhang, L., Xiang, Y., Han, J., Srolovitz, D.J., 2019a. The effect of randomness on the strength of high-entropy alloys. Acta Mater 166, 424-434.

Zhang, M., Yang, S., Wan, F., 2019b. Competition mechanism of brittle-ductile transition of metals under tensile condition. Mech. Mater. 137, 103138.

Zhang, R., Zhao, S., Ding, J., Chong, Y., Jia, T., Ophus, C., Asta, M., Ritchie, R.O., Minor, A.M., 2020. Short-range order and its impact on the CrCoNi medium-entropy alloy. Nature 581, 283–287.

Zhang, X., Gui, Y., Lai, M., Lu, X., Gu, J., Wang, F., Yang, T., Wang, Z., Song, M., 2023a. Enhanced strength-ductility synergy of medium-entropy alloys via multiple level gradient structures. Int. J. Plast. 164, 103592.

Zhang, Y.H., Ma, E., Sun, J., Han, W.Z., 2023b. A unified model for ductile-to-brittle transition in body-centered cubic metals. J. Mater. Sci. Tech. 141, 193–198. Zhang, Z., Ma, Y., Yang, M., Jiang, P., Feng, H., Zhu, Y., Wu, X., Yuan, F., 2024. Improving ductility by coherent nanoprecipitates in medium entropy alloy. Int. J. Plast. 172. 103821.

Zhang, Z., Mao, M.M., Wang, J., Gludovatz, B., Zhang, Z., Mao, S.X., George, E.P., Yu, Q., Ritchie, R.O., 2015. Nanoscale origins of the damage tolerance of the high-entropy alloy CrMnFeCoNi. Nat. Commun. 6, 10143.

Zhao, L.Y., Lv, Z.M., Lai, Y.M., Zhu, Q.Z., Shao, J.F., 2023. A new micromechanical damage model for quasi-brittle geomaterials with non-associated and state-dependent friction law. Int. J. Plast. 165, 103606.

Zhu, Q., Zhao, Q., Huang, Q., Chen, Y., Suresh, S., Yang, W., Zhang, Z., Zhou, H., Gao, H., Wang, J., 2024. Grain boundary plasticity initiated by excess volume. Proc. Natl. Acad. Sci. USA 121, e2400161121.